國 立 交 通 大 學

土木工程學系

博 士 論 文

風浪生成機制的直接數值模擬

Direct numerical simulation of wind-wave generation processes

研究生 ： 林嫩瑛

指導教授 ： 蔡武廷 教授

中華民國九十六年四月

風浪生成機制的直接數值模擬

Direct numerical simulation of wind-wave generation processes

研 究 生： 林嫩瑛　　**Student : Mei-Ying Lin**

指導教授： 蔡武廷　　**Advisor : Wu-Ting Tsai**

國 立 交 通 大 學

土 木 工 程 學 系

博 士 論 文

A Thesis

Submitted to Department of Civil Engineering

College of Engineering

National Chiao Tung University

in Partial Fulfillment of the Requirements

for the Degree of

Doctoral of Philosophy

in

Civil Engineering

April 2007

Hsinchu, Taiwan, Republic of China

中華民國九十六年四月

風浪生成機制的直接數值模擬

研究生： 林嫩瑛　　指導教授： 蔡武廷 教授

國立交通大學
土木工程學系博士班

摘 要

利用直接數值模擬的方法，建立一個空氣與水的耦合紊流模式，並以此耦合紊流模式探討風浪的生成機為本論文的研究重點。其中風浪的生成機制可因風速的不同而不同，我們僅以低風速下產生的風浪為研究範疇。在考慮低風速的情況下，水面上得到的平均風應力約為 0.089 dyn cm^{-2}，依此平均風應力而得到的空氣和水的摩擦速度，分別約為 8.6 cm s^{-1} 和 0.3 cm s^{-1}。由於此空氣與水的耦合紊流模式，在空氣與水的介面上，同時滿足速度與應力連續的條件，所以這個耦合模式可以同時捕捉到空氣與水體的運動和它們之間的交互作用。研究顯示，發展最快之波浪的波長與實驗的量測結果很接近，波長約為 8~12 公分。而且，在波浪生成之後，因波浪成長速率的不同，可分為線性與指數成長兩階段，也與理論和觀測的結果相同。但是，受限於在空氣與水的介面處使用了線性的邊界條件，因此當波浪的梯度大於 0.01 時，即無法再利用此耦合模式繼續進行模擬。模擬的時間間隔，約為波浪開始生成之後 70 秒內的發展過程。波浪生成之後，我們分析了波浪對空氣與水體中紊流場的影響；也執行了一些敏感性測試，包括水體中的紊流場、表面張力和空氣的高度。藉由與理論的結果比較，在線性的成長階段，我們的波浪成長率只有在較高的空氣高度的算例中，與 Phillips (1957) 的理論預測較一致；在指數的成長階段，有些的波浪成長率與 Belcher & Hunt (1993)的理論預測、Plant (1982)所統計的實驗觀測和一些數值模擬的結果一致。但是，有些波浪的成長率則較前人的研究結果大 2~3 倍。雖然在量的比較上與前人的結果有些許的差異，但是在風浪生成機制的定性條件上，和 Phillips (1957)與 Belcher & Hunt (1993)所提的機制是符合的。風的能

量能夠傳輸至波浪的主要因素：在線性的波浪成長階段，如 Phillips (1957)所提的機制一樣，來自紊流所引起的壓力擾動；在指數的波浪成長階段，如 Belcher & Hunt (1993)所提的機制一樣，來自波浪所引起的壓力擾動與波浪之間所形成的形狀阻力。

Direct numerical simulation of wind-wave generation processes

Student : Mei-Ying Lin Advisor : Professor Wu-Ting Tsai

Department of Civil Engineering

National Chiao Tung University

ABSTRACT

An air-water coupled model is developed to investigate wind-wave generation processes at low wind speed where the surface wind stress is about $0.089\,\mathrm{dyn\,cm^{-2}}$ and the associated surface friction velocities of the air and the water are $u_a^* \sim 8.6\,\mathrm{cm\,s^{-1}}$ and $u_w^* \sim 0.3\,\mathrm{cm\,s^{-1}}$, respectively. The air-water coupled model satisfies continuity of velocity and stress at the interface simultaneously, and hence can capture the interaction between air and water motions. Our simulations show that the wavelength of the fastest growing waves agrees with laboratory measurements $(\lambda \sim 8-12\,\mathrm{cm})$ and the wave growth consists of linear and exponential growth stages as suggested by theoretical and experimental studies. Constrained by the linearization of the interfacial boundary conditions, we perform simulations only for a short time period, about 70s; the maximum wave slope of our simulated waves is $ak \sim 0.01$ and the associated wave age is $c/u_a^* \sim 5$, which is a slow moving wave. The effects of waves on turbulence statistics above and below the interface are examined. Sensitivity tests are carried out to investigate the effects of turbulence in the water, surface tension, and the numerical depth of the air domain. The growth rates of the simulated waves are compared to Phillips' (1957) theory for linear growth and to Plant's (1982) experimental data and previous simulation results for exponential growth. In the exponential growth stage, some of the simulated wave growth rates are comparable to previous studies, but some are about 2~3 times larger than previous studies. In the linear growth stage, the simulated wave growth rates are sensitive to the numerical depth of the air domain, and are comparable to Phillips'

prediction only for the larger air domain. In qualitative agreement with the theories proposed by Phillips (1957) and Belcher and Hunt (1993) for slow moving waves, the mechanisms for the energy transfer from wind to waves in our simulations are mainly from turbulence-induced pressure fluctuations in the linear growth stage and due to the in-phase relationship between wave slope and wave-induced pressure fluctuations in the exponential growth stage, respectively.

ACKNOWLEDGEMENTS

I would like to express my sincere gratitude to Wu-Ting Tsai on the development of air-water coupled model and Chin-Hoh Moeng on the study of wind-wave generation processes and English writing for their truly excellent guidance and support during the past few years. Their outstanding ability for research and providing good education for student help me to achieve more than I ever thought possible. With their discreet and careful guard contributes to the accomplishment of this work. I would like to thank Wu-Ting again for the chance he gave me to study with Chin-Hoh at NCAR in U.S.A for one and half year. During that period, discussing some scientific questions with other scientists or attending a lot of seminars helped me to learn more about scientific work and induced the enthusiasm for research inside me. A special thanks goes to Peter Sullivan for his useful comments and suggestions about the wind-wave generation processes on this work. Peter also provided some data of measurements and simulation results as shown in figure 20 of this thesis. Thanks to Stephen Belcher who provides some comments on theoretical studies of wind-wave generation processes. I would also like to thank the members of my committee, Ching-Yuang Huang, Keh-Chia Yeh, Wu-Shung Fu, Wen-Yih Sun, for their comments and suggestions on my work.

Thanks to Wu-Ting's research group. Those experiences we shared together become good memories in my mind. A special thanks to Shi-Ming Chen for helping me to deal with my computer.

Thanks to my friends for bringing me a lot of joy and enriching my life.

Thanks to my family's great support and encouragement.

This work was mainly supported by grants from the National Science Council of Taiwan under contract numbers NSC 90-2611-M-009-001 and 91-2611-M-008-002, and a part of this study was sponsored by the National Science Foundation through the National Center for Atmospheric Research.

TABLE OF CONTENTS

LIST OF TABLES

LIST OF FIGURES

LIST OF SYMBOLS

a	Wave amplitude	L
b	A constant related to surface roughness length	-
c	Phase velocity	$L\,T^{-1}$
E	Wave energy density	$M\,T^{-2}$
D_p	Form stress; Form drag	$M\,L^{-1}\,T^{-2}$
g	Gravitational acceleration	LT^{-2}
h	Height	L
H_ℓ	The divergence of the convective and diffusive terms	$M\,L^{-3}\,T^{-2}$
k	Wavenumber $k=\sqrt{k_x^2+k_y^2}$	L^{-1}
k_x, k_y	Wavenumber components	L^{-1}
L_x, L_y	Horizontal length components	L^{-1}
N_x, N_y, N_z	Grid point components	-
p	Pressure	$M\,L^{-1}\,T^{-2}$
p_a	Pressure of the air	$M\,L^{-1}\,T^{-2}$
p'_a	Pressure fluctuations of the air	$M\,L^{-1}\,T^{-2}$
p_w	Pressure of the water	$M\,L^{-1}\,T^{-2}$
p'_w	Pressure fluctuations of the water	$M\,L^{-1}\,T^{-2}$
Re_a	Reynolds number of the air	-
Re_w	Reynolds number of the water	-
Re_a^*	Wall Reynolds number of the air	-
Re_w^*	Wall Reynolds number of the water	-
t	Time	T
u,v,w	Cartesian velocity components	$L\,T^{-1}$
u_a, v_a, w_a	Cartesian velocity components of the air	$L\,T^{-1}$
u_w, v_w, w_w	Cartesian velocity components of the water	$L\,T^{-1}$
u'_a, v'_a, w'_a	Cartesian velocity fluctuations components of the air	$L\,T^{-1}$

u'_w, v'_w, w'_w	Cartesian velocity fluctuations components of the water	$L\,T^{-1}$
u^*_a	Friction velocity of the air	$L\,T^{-1}$
u^*_w	Friction velocity of the water	$L\,T^{-1}$
U_a	Mean velocity of the air	$L\,T^{-1}$
U_w	Mean velocity of the water	$L\,T^{-1}$
U_s	Mean current at the interface	$L\,T^{-1}$
U_o	Constant velocity imposed at upper boundary	$L\,T^{-1}$
U_c	Convection speed of pressure fluctuations	$L\,T^{-1}$
U^+	Non-dimensional wall velocity	-
x,y,z	Cartesian coordinates	L
z^+	Non-dimensional wall coordinate	-
z_0^+	Surface roughness	-
$\Delta x, \Delta y, \Delta z$	Grid size components	L
$\Delta x_a^+, \Delta y_a^+$	Horizontal grid size of the air in wall units	-
$\Delta x_w^+, \Delta y_w^+$	Horizontal grid size of the water in wall units	-
α_ℓ	Coefficient of thermal expansion	$^oK^{-1}$
β	Dimensionless wave growth rate	-
β^*	Wave growth rate	T^{-1}
ε	Dissipation rate	$L^2\,T^{-3}$
γ	Surface tension	$M\,T^{-2}$
η	Surface wave height	L
κ	Von Karman constant	-
λ	Wavelength	L
μ_a	Dynamic viscosity of the air	$M\,L^{-1}\,T^{-1}$
μ_w	Dynamic viscosity of the water	$M\,L^{-1}\,T^{-1}$
ν_a	Kinematic viscosity of the air	$L^2\,T^{-1}$
ν_w	Kinematic viscosity of the water	$L^2\,T^{-1}$
ρ_a	Density of the air	$M\,L^{-3}$

ρ_w	Density of the water	$M L^{-3}$
σ	Wave radian frequency	T^{-1}
τ	Surface shear stress	$M L^{-1} T^{-2}$
τ'	Surface shear stress fluctuations	$M L^{-1} T^{-2}$
τ_s	Mean surface shear stress	$M L^{-1} T^{-2}$
υ	Root-mean-square fluctuating speed	$L T^{-1}$
ξ	Theoretical prediction of surface wave height	L
ζ	Kolmogorov microscale	L
K	Thermal diffusivity	L^2T^{-1}
θ_a°	Reference temperature of the air	^oK
θ_w°	Reference temperature of the water	^oK
θ_a	Temperature of the air	^oK
θ_w	Temperature of the water	^oK
$\hbar_a$	Thermal conductivity of the air	$JT^{-1}L^{-1o}K^{-1}$
$\hbar_w$	Thermal conductivity of the water	$JT^{-1}L^{-1o}K^{-1}$
C_p^a	Heat capacity of the air	$JM^{-1o}K^{-1}$
C_p^w	Heat capacity of the water	$JM^{-1o}K^{-1}$

Chapter I

Introduction

As wind flows over a water surface, air and water motions interact and induce many phenomena at the interface. Wind-generated waves are the most visible signature of this interaction and play a major influence on the momentum and energy transfer across the interface. These wind-generated waves, observed by microwave-radar backscatter, have wavelengths of the order of 4-40 cm (Massel, 1996). Because these small-scale waves impact remote sensing of the sea surface, the generation and growth of wind-generated waves have been subjects of intense research. However, the mechanisms that generate these surface waves are still an open issue due to (1) difficulties in obtaining a dataset from laboratory and field measurements that records the time evolution of motions in both atmosphere and ocean domains, (2) mathematical difficulties in dealing with highly turbulent flows over complex moving surfaces, and (3) lack of a suitable coupled model to simulate turbulent flows in both atmosphere and ocean simultaneously. With increases in computer power, it is now possible to simulate wave and turbulence phenomenon by direct numerical simulation (DNS). DNS numerically solves the Navier-Stokes equation subject to boundary conditions and hence such simulated flow fields contain no uncertainties other than numerical errors. In this study we develop an air-water coupled DNS model and use it to study wind-wave generation and growth processes.

Theoretical studies (Jeffreys 1925; Phillips 1957; Phillips & Katz 1961; Miles 1957; Townsend 1972, 1980; Phillips 1977; Jacobs 1987; Kahma & Donelan 1988; van Duin & Janssen 1992 and Belcher & Hunt 1993, among many others) have proposed different mechanisms as to how surface waves are generated from calm water and quantify the consequential growth rate of surface waves. These studies suggest that there are linear and

exponential growth regimes for surface waves.

With the increase of computer power, the numerical simulation (DNS) technique has become a useful tool in studying turbulent flows. Such a numerical simulation, by directly solving the fluid dynamics equations, produces three-dimensional, time evolving flow fields which can be analyzed to study the details of the flow structure and to deduce the turbulence statistics. However, most of the previous numerical studies (Davis 1970; Gent & Taylor 1976; Al-Zanaidi & Hui 1984; De Angelis *et al.* 1997; Henn & Sykes 1999; Sullivan *et al.* 2000; Tsai *et al.* 2005) examine either the wave effect on air motions or the wind stress effect on water motions by simulating only air or water flows (i.e., one-phase flow). These so-called one-phase flow simulations are driven by either wind shear near the surface for turbulence in the air or an imposed surface stress for turbulence in the water. Because the interface is prescribed, the interaction between the wind and the waves is prohibited. Only a few numerical studies are conducted for two-phase flows (Lombardi *et al.* 1996; De Angelis 1998; Fulgosi *et al.* 2003) but none of them investigate the wind-wave generation processes. The present study, therefore, is aimed at unraveling wind-wave generation processes by conducting direct numerical simulations that couple turbulent air and water flows.

The organization of this paper is as follows. The numerical aspects of the present simulation, including the model formulation, numerical method and simulation implementation are described in section 2. The simulated flow structures of surface waves and elongated streaks generated by wind are shown in section 3. The wave effect on the statistics of mean velocity and turbulent intensity is reported in section 4. The characteristics of the generated surface waves are examined in section 5. Two wave growth types are defined in section 6. Comparison with theoretical wind-wave generation mechanisms is given in section 7. The effects of turbulence in the water, surface tension, and the numerical domain in the air side on wave growth are examined in section 8. Finally, the main conclusions of this paper are reported in section 9.

Chapter II

The coupled model

II.1 Flow configuration

Consider two turbulent flows, air and water, under a wind-driven system that interacts across a deformable interface. The turbulent and wave motions must satisfy the continuity of velocity and stress across the interface. As a first step, we simplify the problem by excluding the non-linearity of waves and wave breaking effect and linearized these interfacial boundary conditions via the small amplitude wave assumption. We use the coupled model to study the initial stage of the generation of waves by wind.

First we have to choose the characteristic velocity and length scales of the flow. In the study of a turbulent flow over given water waves, Sullivan *et al.* (2000) chose the constant velocity imposed at the upper boundary and the wavelength of the imposed water wave as the characteristic scales. In the study of turbulent shear flow under a free surface, Tsai *et al.* (2005) used the mean velocity at the free surface and the length of viscous sub-layer given from experimental result (Melville *et al.*, 1998) as their characteristic scales. Flow features are typically characterized by their external condition: a given wave or imposed wind speed, which make it easy to choose the characteristic scales, such as above studies of single-phase turbulent flows. For two-phase flows we investigate here, there are two problems in choosing the characteristic scales. First is due to the deformable interface that is not a fixed wave type. The interface changes with time and varies from place to place. This boundary does not provide any characteristic length for us to define the domain size or the bulk Reynolds number, or to scale the governing equations before we start the simulation. Second problem is

due to the different time and length scales of turbulent motions in air and water. In general, we should use two sets of characteristic variables to measure these two motions. But U_0 is the only characteristic flow feature we know before starting the simulation.

Thus, we consider two turbulent flows (air and water) interacting across a deformable interface under a wind-driven system. Each domain of the two immiscible fluids is a rectangular box with a depth h and horizontal length $(L_x, L_y) = 6h$, as shown in figure 1. We adopt a Cartesian coordinate where the air region occupies the $z \geq 0$ domain, and the water region the $z \leq 0$ domain. The horizontal coordinates x and y are in the streamwise and spanwise directions, respectively. The external forcing of the system is a constant velocity U_0 imposed at the upper boundary ($z = h$) in the air region, i.e., similar to a Couette flow. We set $U_0 = 3\,\mathrm{m\,s^{-1}}$ in this study.

II.2 Governing equations

The mass and momentum conservation equations for incompressible, Newtonian fluids of air and water with density ρ_ℓ and kinematic viscosity ν_ℓ are

$$\nabla \cdot \boldsymbol{u}_\ell = 0, \tag{2.1}$$

$$\frac{\partial \boldsymbol{u}_\ell}{\partial t} + \boldsymbol{u}_\ell \cdot \nabla \boldsymbol{u}_\ell = -\frac{1}{\rho_\ell} \nabla p_\ell + \nu_\ell \nabla^2 \boldsymbol{u}_\ell, \tag{2.2}$$

where the subscript ℓ denotes variables in air ($\ell = a$) or water ($\ell = w$), $\boldsymbol{u} = (u, v, w)$ are velocity components in streamwise, spanwise and vertical directions respectively, and p_ℓ is the pressure.

The Poisson equation for p_ℓ is obtained by taking the divergence of (2.2) and using (2.1)

$$\frac{\partial^2 p_\ell}{\partial x^2} + \frac{\partial^2 p_\ell}{\partial y^2} + \frac{\partial^2 p_\ell}{\partial z^2} = H_\ell, \tag{2.3}$$

where the source term H_ℓ is the divergence of the convective and diffusive terms in

equation (2.2). The solution of (2.3) forces the continuity equation (2.1) to be satisfied at each time step.

II.3 Boundary conditions

The domains of the two immiscible fluids have six external boundaries and one internal deformable interface. For external boundaries, periodic conditions are assumed on the four sidewalls of the computational domain. At the top of the domain, $z = h$, a constant-velocity condition is applied as

$$u_a = U_0 , \quad v_a = 0 , \quad w_a = 0 , \quad \frac{\partial p_a}{\partial z} = 0 . \tag{2.4}$$

At the lower bottom of the water region, $z = -h$, we impose free-slip boundary conditions

$$\frac{\partial u_w}{\partial z} = 0 , \quad \frac{\partial v_w}{\partial z} = 0 , \quad w_w = 0 , \quad \frac{\partial p_w}{\partial z} = 0 , \tag{2.5}$$

to emulate an infinite depth.

For the deformable boundary, the interface of two viscous fluids must satisfy the following requirements as stated in Wehausen & Laitone (1960):

1. The effect of surface tension as one passes through the interface is to produce a discontinuity in the normal stress proportional to the mean curvature of the boundary surface.

2. For viscous fluids the tangential stress must be continuous as one passes through the interface.

3. For viscous fluids the tangential component of the velocity must be continuous as one passes through the interface.

Without simplification, these requirements lead to complicated boundary conditions (see equations 3.2~3.6 in Wehausen & Laitone, 1960). However, assuming small interfacial deformation, as in the initial wind-wave generation processes considered here, we can linearize the interfacial conditions (Tsai & Yue, 1995), which yields boundary conditions

satisfied at $z = 0$ as follows:

$$u_a = u_w, \quad v_a = v_w, \quad w_a = w_w, \tag{2.6}$$

$$\mu_a\left(\frac{\partial u_a}{\partial z} + \frac{\partial w_a}{\partial x}\right) = \mu_w\left(\frac{\partial u_w}{\partial z} + \frac{\partial w_w}{\partial x}\right), \tag{2.7}$$

$$\mu_a\left(\frac{\partial v_a}{\partial z} + \frac{\partial w_a}{\partial y}\right) = \mu_w\left(\frac{\partial v_w}{\partial z} + \frac{\partial w_w}{\partial y}\right), \tag{2.8}$$

$$\begin{aligned} & p_w - \rho_w g\eta + 2\mu_w\left(\frac{\partial u_w}{\partial x} + \frac{\partial v_w}{\partial y}\right) \\ & - p_a + \rho_a g\eta - 2\mu_a\left(\frac{\partial u_a}{\partial x} + \frac{\partial v_a}{\partial y}\right) = -\gamma\left(\frac{\partial^2\eta}{\partial x^2} + \frac{\partial^2\eta}{\partial y^2}\right) \end{aligned}, \tag{2.9}$$

where $\mu_a \equiv \rho_a \nu_a$ and $\mu_w \equiv \rho_w \nu_w$ are dynamic viscosities of air and water, and γ is the surface tension of the water interface. The linearized kinematical condition satisfied at *z = 0* is

$$\frac{\partial \eta}{\partial t} + \frac{\partial (u\eta)}{\partial x} + \frac{\partial (v\eta)}{\partial y} = w. \tag{2.10}$$

The use of a central-differencing scheme at the interface requires additional points (ghost points) below the interface for (u_a, v_a, w_a, p_a) and above the interface for (u_w, v_w, w_w, p_w), as shown in figure 2. The (u_a, v_a, u_w, v_w) values at the ghost points are determined using the continuity conditions for velocity (2.6) and tangential stresses (2.7 and 2.8). (w_a, w_w) at the ghost points are determined by two additional conditions: Applying the continuity equation (2.1) and the boundary conditions (2.6) at $z = 0$ results in the condition

$$\frac{\partial w_a}{\partial z} = \frac{\partial w_w}{\partial z}. \tag{2.11}$$

A second condition is obtained by adding the *x*-derivative of (2.7) and the *y*-derivative of (2.8) (Chandrasekhar, 1954), leading to

$$\mu_a\left(\frac{\partial^2 w_a}{\partial x^2} + \frac{\partial^2 w_a}{\partial y^2} + \frac{\partial^2 w_a}{\partial z^2}\right) = \mu_w\left(\frac{\partial^2 w_w}{\partial x^2} + \frac{\partial^2 w_w}{\partial y^2} + \frac{\partial^2 w_w}{\partial z^2}\right). \tag{2.12}$$

The pressure (p_a, p_w) at the ghost points is determined by applying the normal stress condition (2.9) and the continuity condition for the vertical velocity (2.6) to the vertical

component of the momentum equation at the interface, which results in

$$\begin{aligned} &-\frac{1}{\rho_a}\frac{\partial p_a}{\partial z}-\frac{\partial(u_a w_a)}{\partial x}-\frac{\partial(v_a w_a)}{\partial y}-\frac{\partial(w_a w_a)}{\partial z}+\nu_a\left(\frac{\partial^2 w_a}{\partial x^2}+\frac{\partial^2 w_a}{\partial y^2}+\frac{\partial^2 w_a}{\partial z^2}\right) \\ &=-\frac{1}{\rho_w}\frac{\partial p_w}{\partial z}-\frac{\partial(u_w w_w)}{\partial x}-\frac{\partial(v_w w_w)}{\partial y}-\frac{\partial(w_w w_w)}{\partial z}+\nu_w\left(\frac{\partial^2 w_w}{\partial x^2}+\frac{\partial^2 w_w}{\partial y^2}+\frac{\partial^2 w_w}{\partial z^2}\right) \end{aligned} . \qquad (2.13)$$

II.4 Numerical method

The aim of our coupling algorithm is to simulate the air and water flows simultaneously. Most of previous coupled simulations used iterative methods (e.g., Lombardi *et al.*, 1996), which determine the interfacial variables on air side or water side using different continuity conditions by imposing continuity of velocity on the air side and continuity of stress on the water side. Then the calculation is iterated until two continuity conditions are satisfied on both sides. This iterative method is time consuming. Lombardi *et al.* (1996) simplified the iteration by using a fractional time step method, which uses only the first step of the iterative scheme, to study their coupled gas-liquid flow. But then the continuity condition is not satisfied exactly with this fractional time step method. Thus we develop a new model to study the coupling problem.

The numerical method used to solve the system of equations (2.2) and (2.3) subject to the boundary conditions (2.4)~(2.10) is based on the scheme described by Tsai (1998) and Tsai *et al.* (2005). We use a staggered grid in the vertical as shown in figure 2 where the grids are stretched with finer resolution near the interface as in Tsai *et al.* (2005). We use a pseudo-spectral method to evaluate x and y derivatives, second-order finite-difference scheme for z derivatives, and a second-order Runge-Kutta method (Spalart *et al.*, 1991) for time integration.

We use $(N_x, N_y, N_z) = (64, 64, 65)$ gridpoints in each of the air and water domains. The domain size in both x and y directions is $24\,\text{cm}$. In the water, the horizontal grid size in wall units is $\Delta x_w^+ = \Delta y_w^+ = \Delta y_w u_w^* / \nu_w = 11.25$, where the water friction velocity u_w^* is

given in section 2.5. Near the interface the stretched vertical grid adequately resolves the viscous layer. There are 14 grids in the near surface region $\left(-z_w^+ \le 10\right)$. In the air domain, the corresponding non-dimensional horizontal spacings are $\Delta x_a^+ = \Delta y_a^+ = 21.4$, and there are ten gridpoints within the region $z_a^+ \le 10$ in the vertical direction near the interface.

As suggested by Moin & Mahesh (1998), the grid resolution requirements for spectral method of boundary layer flow in *x* (streamwise) and *y* (spanwise) and second-order central difference scheme in *z* are $(\Delta x, \Delta y, \Delta z) = (14.3, 4.8, 0.26)\zeta$ where $\zeta = \left(\nu_a^3/\varepsilon\right)^{1/4}$ is the Kolmogorov microscale, $\varepsilon \sim \upsilon^3/h$ is dissipate rate and $\upsilon = \left(u_a'^2 + v_a'^2 + w_a^2\right)^{1/2}$ is root-mean-square fluctuating speed. For our grid system, the Kolmogorov microscale is $\zeta \sim 0.025$ cm, the horizontal spacing is 0.375 cm and the vertical spacing near the interface is about 0.01 cm. This spatial resolution is close to the requirements suggested by Moin & Mahesh (1998).

II.5 Initialization

The simulation flow field is initiated in four steps. First, we assign the mean velocity profile of the coupled air-water flow based on the analytical solution of laminar, transient flow (Choy & Reible 2000) at the time when the mean velocity at the interface reaches $8\,\mathrm{cm\,s^{-1}}$. Second, we spin up the turbulence by adding small random perturbations in the air and water temperature fields to the buoyancy force in the *w* momentum equation. (The buoyancy force induces a quick spin-up to a turbulent state.) For this air-water coupled model, it takes about 120 large-eddy turnover time units $(U_0 t/h)$ to spin up the turbulence. Third, we turn off the buoyancy force in the *w* momentum equation and continue the spin-up simulation for another 2400 large-eddy turnover time units to reach a pure shear-driven state. The criterion for established pure shear-driven flow is determined by comparing the near-surface velocity variances in the air and water domains to the shear turbulent flow above a flat boundary reported in Sullivan *et al.* (2000) and the shear-driven turbulent water flow in Tsai *et al.*

(2005). Finally, we start our simulation from this fully developed shear-driven turbulent flow by allowing the flat interface to deform. All results shown below are from this final stage.

Figure 3 shows the time evolution of the mean shear stress τ_s at the interface after the interface is allowed to evolve. For the time interval $t < 50\,\mathrm{s}$, the mean interfacial stress τ_s remains at a nearly constant value of $0.089\,\mathrm{dyn\,cm^{-2}}$, implying that our simulation has reached a statistically quasi-steady state in response to the wind forcing. The associated friction velocities in the air and water are $u_a^* = \sqrt{\tau_s/\rho_a} \approx 8.56\,\mathrm{cm\,s^{-1}}$ and $u_w^* = \sqrt{\tau_s/\rho_w} \approx 0.3\,\mathrm{cm\,s^{-1}}$, respectively. The ratio of u_a^*/U_0 is hence about 0.03. For $t > 50\,\mathrm{s}$, the mean interfacial stress smoothly increases due to the growth of surface waves. We discuss the properties of the generated waves in section 6.

The total *u* momentum flux in the air is

$$\nu_a \frac{\partial U_a}{\partial z} - \langle u_a' w_a' \rangle = u_a^*. \tag{2.14}$$

Figure 4 shows the vertical distributions of viscous, turbulence, and total momentum flux. As requital for a Couette flow under a steady condition, the total mean vertical momentum flux is nearly constant with height.

The bulk Reynolds number of the air flow ($Re_a \equiv U_0 h/\nu_a$) is about 8000. This value is the same as that in the turbulent Couette flow simulation of Sullivan *et al.* (2000). The simulated turbulence, therefore, is considered to be fully developed. The associated wall Reynolds number ($Re_a^* \equiv u_a^* h/2\nu_a$) is about 115. Our wall Reynolds number is about 12 % less than that of Sullivan *et al.* (2000). In the water, the bulk Reynolds number ($Re_w \equiv U_s h/\nu_w$) is about 2000, where $U_s \approx 10\,\mathrm{cm\,s^{-1}}$ is the mean velocity at the interface. The corresponding wall Reynolds number ($Re_w^* \equiv u_w^* h/2\nu_w$) is about 60, which is comparable to that in the simulations reported by Lombardi *et al*. (1996) and Tsai *et al.* (2005).

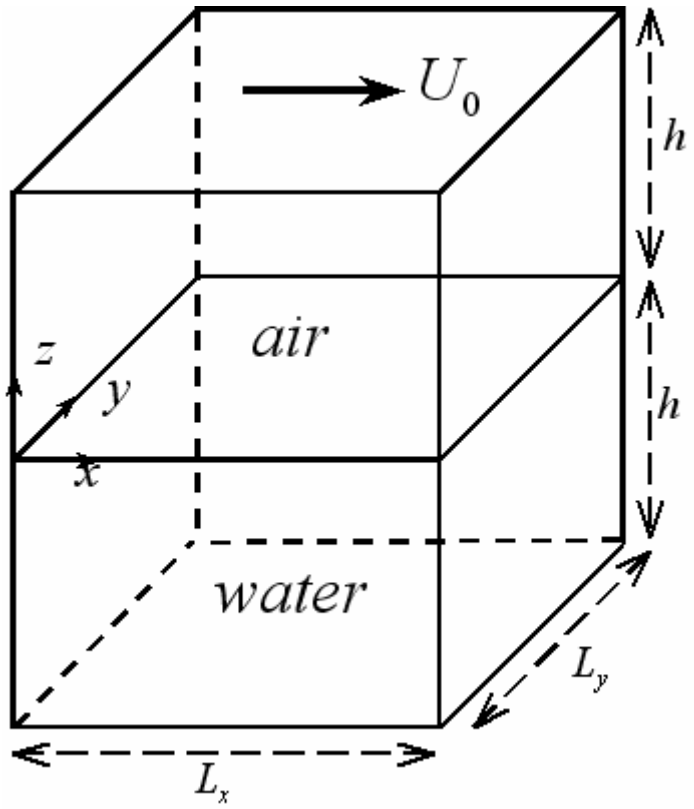

Figure 1. Numerical domain of two immiscible turbulent flows driven by velocity U_0 on a Cartesian coordinate. The interface of air and water is located at $z = 0$. The size of air and water sub-domains is the same, $(L_x, L_y, h) = (6, 6, 1)h$.

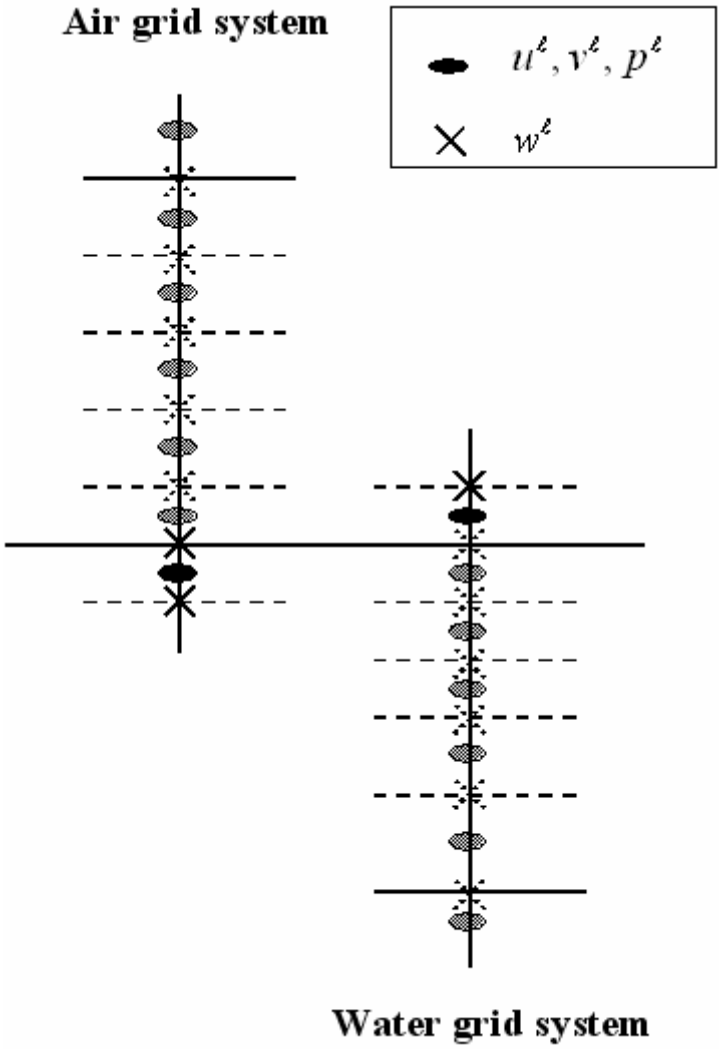

Figure 2. Location of velocity components and pressure on staggered grid systems for the mixed finite-differencing and pseudospectral scheme. Symbols with solid circle and cross are ghost points at the interface.

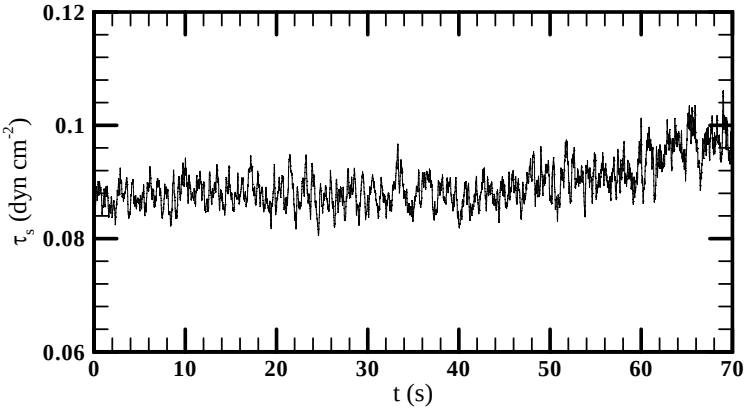

Figure 3. Time evolution of the mean wind stress τ_s at the interface.

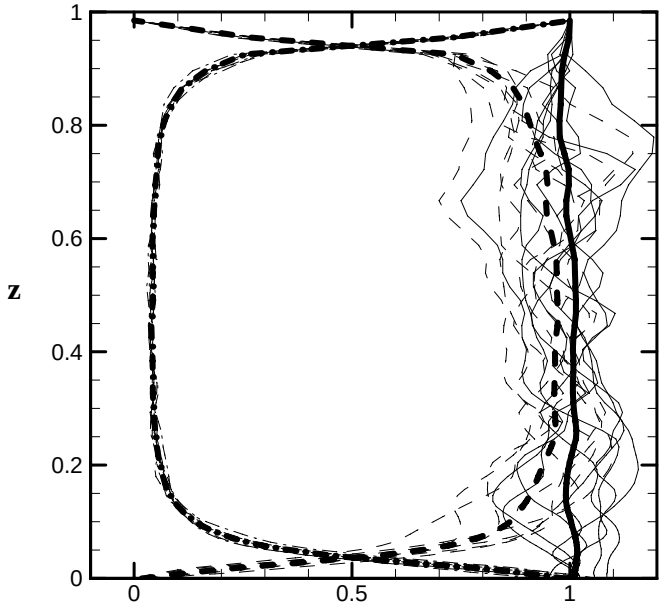

Figure 4. Vertical profiles of dimensionless mean vertical turbulent flux $-\langle u_a' w_a' \rangle / \left(u_a^*\right)^2$ (thick dashed line), viscous flux $\left(\nu_a / u_a^* h\right) \partial U_a / \partial z$ (thick dash-dotted line), and their sum (thick solid line) in the air. The thin lines represent these terms at various time instances during 50 to 70 s, while the thick lines are their averages.

Chapter III

Flow visualization

III.1 Waves and streaks

Waves and streaks are frequently observed phenomena at the air-water interface; they are also found in our numerical simulation results. Figure 5 shows contour distributions of the interface elevation $\eta(x, y, t)$ and the streamwise velocity $u_w(x, y, z = 0, t)$ at three representative time instances $t = 2.6$, 16 and 64 s. The results show that the surface waves grow in time in our simulation (figures 5*a*-*c*). High-speed streaks are observed before the initiation of surface waves (figures 5*d*, 5*e*). When the wave motion is weak, the structure of the high-speed streaks (figure 5*d*) is similar to that observed by Tsai *et al.* (2005) in which a stress-driven free-surface turbulent shear flow is considered. Low-speed streaks in the air flow near the interface (figure 6*a*) are also observed. The low-speed streaky structure is similar to that commonly observed in a turbulent boundary layer next to a stationary, no-slip boundary (e.g. Kim *et al.* 1987). When the wave motion becomes significant, both velocity structures on the interface and within the sublayer of the air side are re-organized and correlate with the waveform (figures 5*f* and 6*b*).

Figure 7 shows isosurfaces of the vertical velocity in the water at two representative time instances before and after the generation of the surface waves. When surface waves are weak, as shown in figure 7(*a*), the flow is shear dominated and the distributions of ejections and sweeps are irregular. However, when the flow becomes wave dominated, the vertical velocity distributions align with the waves (figure 7*b*).

In the air side, the wave effect on the air velocity field is not as significant as that in

the water and confined to within the viscous sublayer as shown in figures 8(*a-c*). But for the air pressure field (figures 8*d-f*), the wave effect can extend outside the viscous sublayer when the interface is wave dominated. These different responses of the velocity and the pressure fields to the surface waves were also observed by Sullivan *et al.* (2000).

III.2 Pressure and stress fields

Figure 9 shows two representative distributions of the fluctuating air and water pressures, p_a' and p_w', at the interface, and the distribution of surface wave elevation. At the early stage when surface waves are weak, pressure fluctuations in the air (figure 9*a*) exhibit no correlation with the surface wave elevation (figure 9*b*), but pressure fluctuations in the water (figure 9*c*) already reveal a high correlation with the surface waves. This suggests that in the early stage of wind-wave generation, pressure fluctuations in the water are driven almost passively by surface waves, and the turbulence in the water may not play an important role in generating waves. In section 8, a numerical experiment is designed to test the impact of water turbulence on wind-wave generation processes. When wave motions dominate (figures 9*d-f*), the pressure fluctuations in both the air and water are highly correlated with the surface wave elevation. At this stage, the air pressure fluctuations show a slight phase shift relative to the surface waves, and the region of maximum (minimum) pressure occurs on the backward (forward) face of the surface wave near the crest (trough), as observed by Sullivan *et al.* (2000). Belcher *et al*. (1993) term this phenomenon non-separated sheltering. Also, the pressure fluctuations in the air (figure 9*d*) are less regular than those in the water (figure 9*f*), implying turbulence-induced pressure fluctuations in the air are more active than that in the water.

Figure 10 shows shear stress fluctuations at the interface at early (figure 10*a*) and late (figure 10*b*) stages of wave growth. Similar to the pressure field in the air, the shear stress field reveals a wave-induced component only when the waves become strong. The

wave-induced shear-stress fluctuations also exhibit a phase shift relative to the surface wave elevation. The contribution of wave-induced pressure and shear stress fluctuations to wave growth is discussed in Section 7.2.

The wave effect on the pressure fields in the vertical direction can also be seen in the vertical distributions of pressure fluctuations at $t = 16\,\mathrm{s}$ (figures 11*a-c*) and 66 s (figures 11*d-f*). At $t = 66\,\mathrm{s}$, pressure fluctuations in the air and water are influenced by waves, and the wave effect extends outside the viscous sublayer. At $t = 16\,\mathrm{s}$, pressure fluctuations in the air are not related to the wave motions, but pressure fluctuations of the water are already highly correlated with waves. Simultaneous animations of η and p_a' show that at early time pressure fluctuations in the air usually sweep over the water surface with varying speeds without interacting with the wave motions, but at late time p_a' becomes well correlated with the surface waves. This suggests different wave generation processes at early and late times. We discuss this in more detail in section 7.

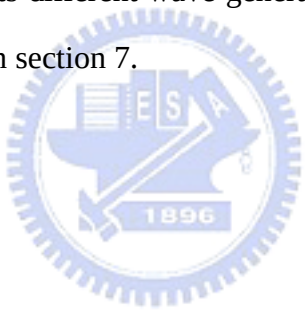

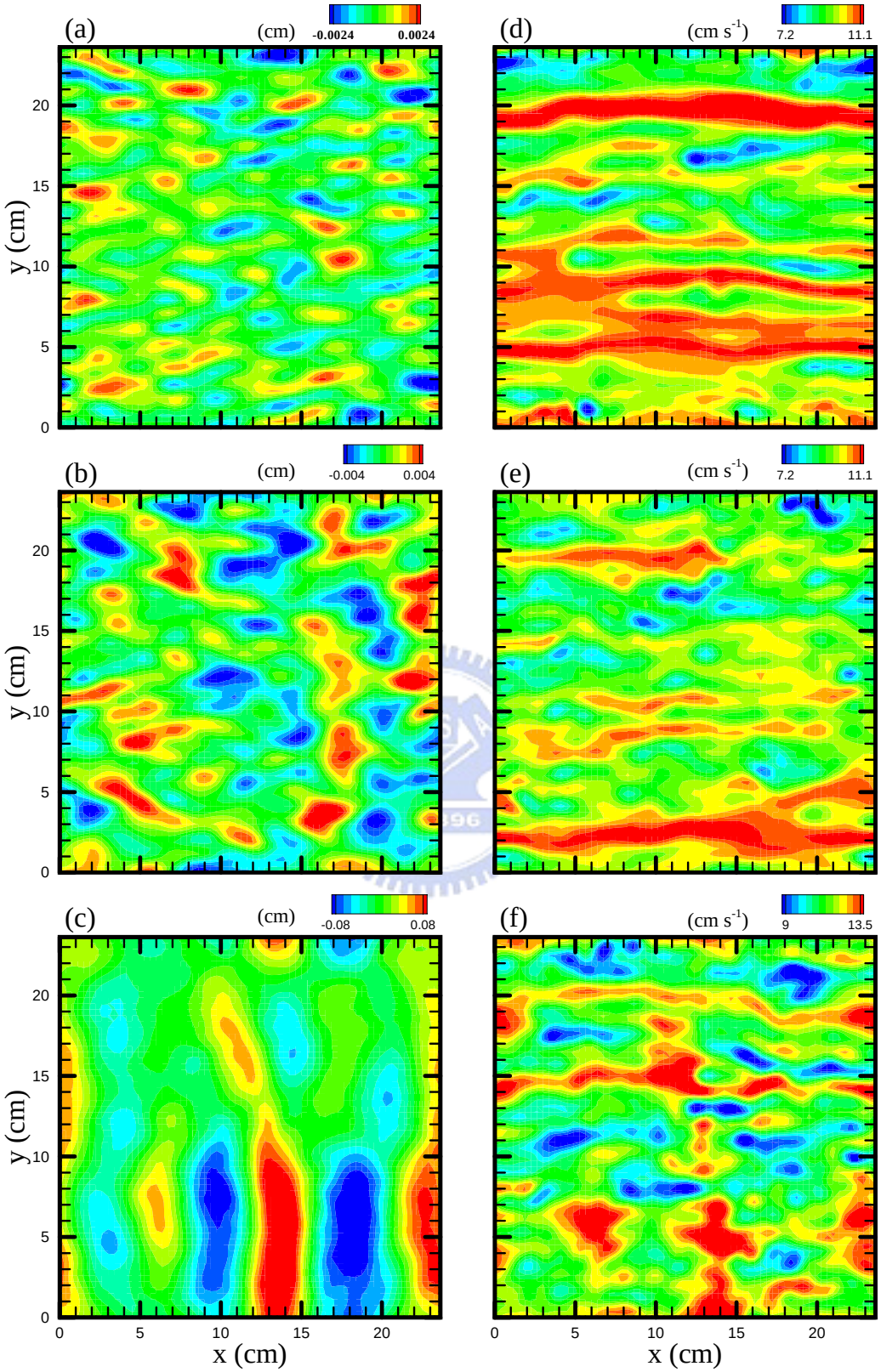

Figure 5. Snapshots of the instantaneous surface wave height η (left panels) and streamwise velocity u at the interface (right panels) at time $t = 2.6\,\mathrm{s}$, $16\,\mathrm{s}$ and $64\,\mathrm{s}$ (from top to bottom), respectively.

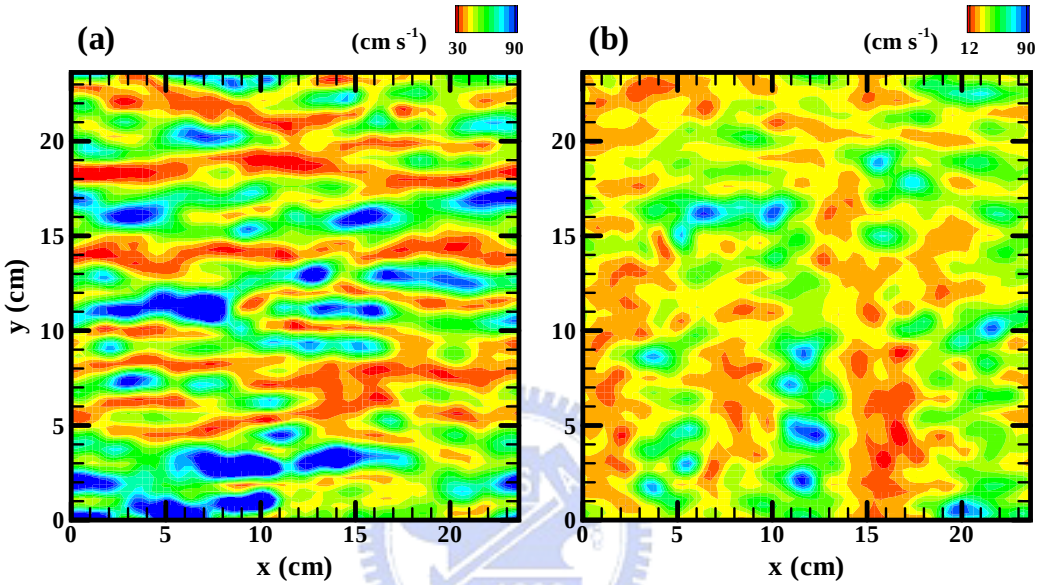

Figure 6. Snapshots of the instantaneous streamwise velocity u_a within the viscous sublayer of the air domain at time $t = 2.6\,\mathrm{s}$ (*a*) and $64\,\mathrm{s}$ (*b*).

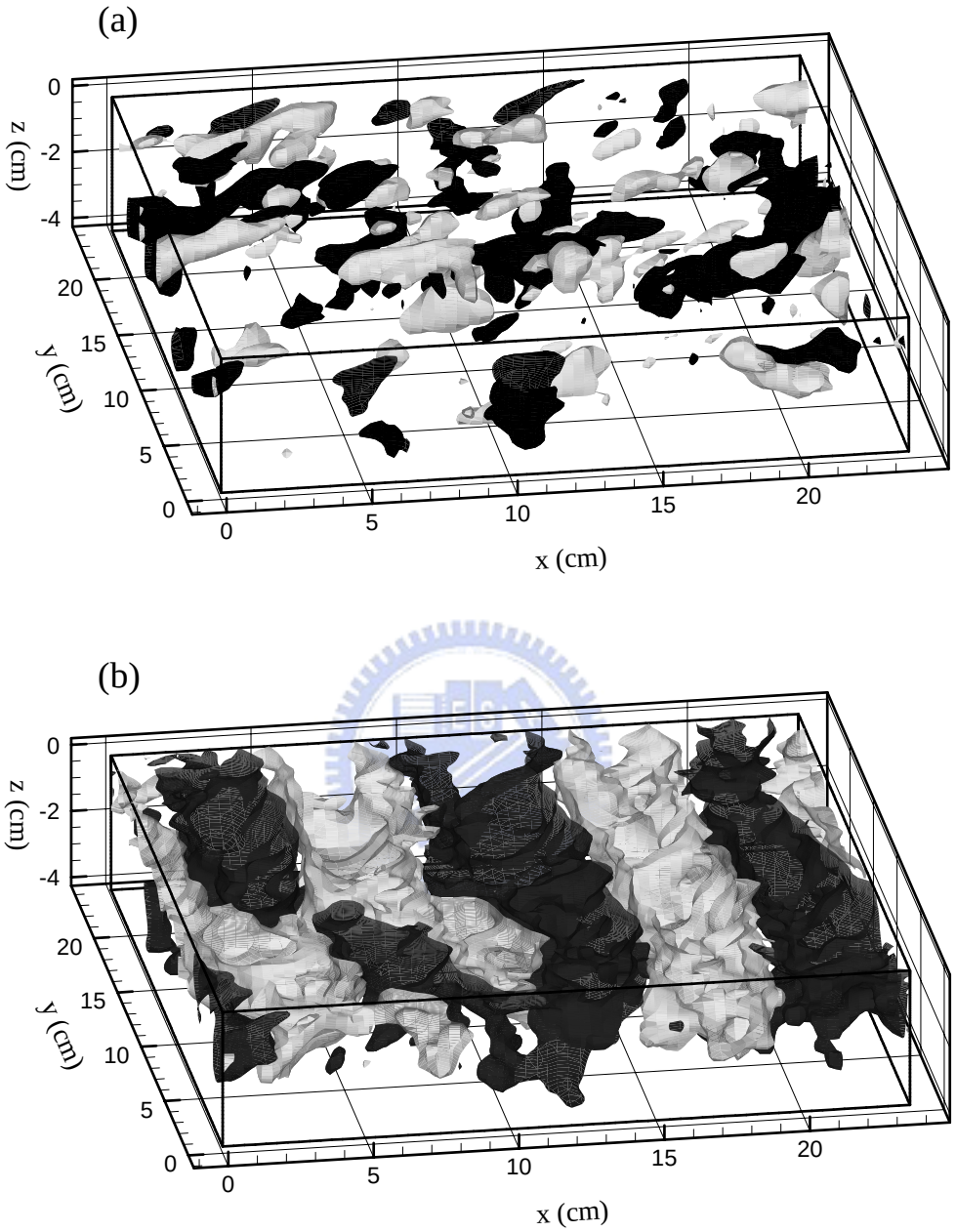

Figure 7. Representative iso-surfaces of vertical velocity in the water at time $t = 2.6\,\mathrm{s}$ (*a*) and $t = 66\,\mathrm{s}$ (*b*). Black and grey iso-surfaces show vertical velocity for values $-1.5\,\mathrm{cm\,s^{-1}}$ and $1.5\,\mathrm{cm\,s^{-1}}$, respectively.

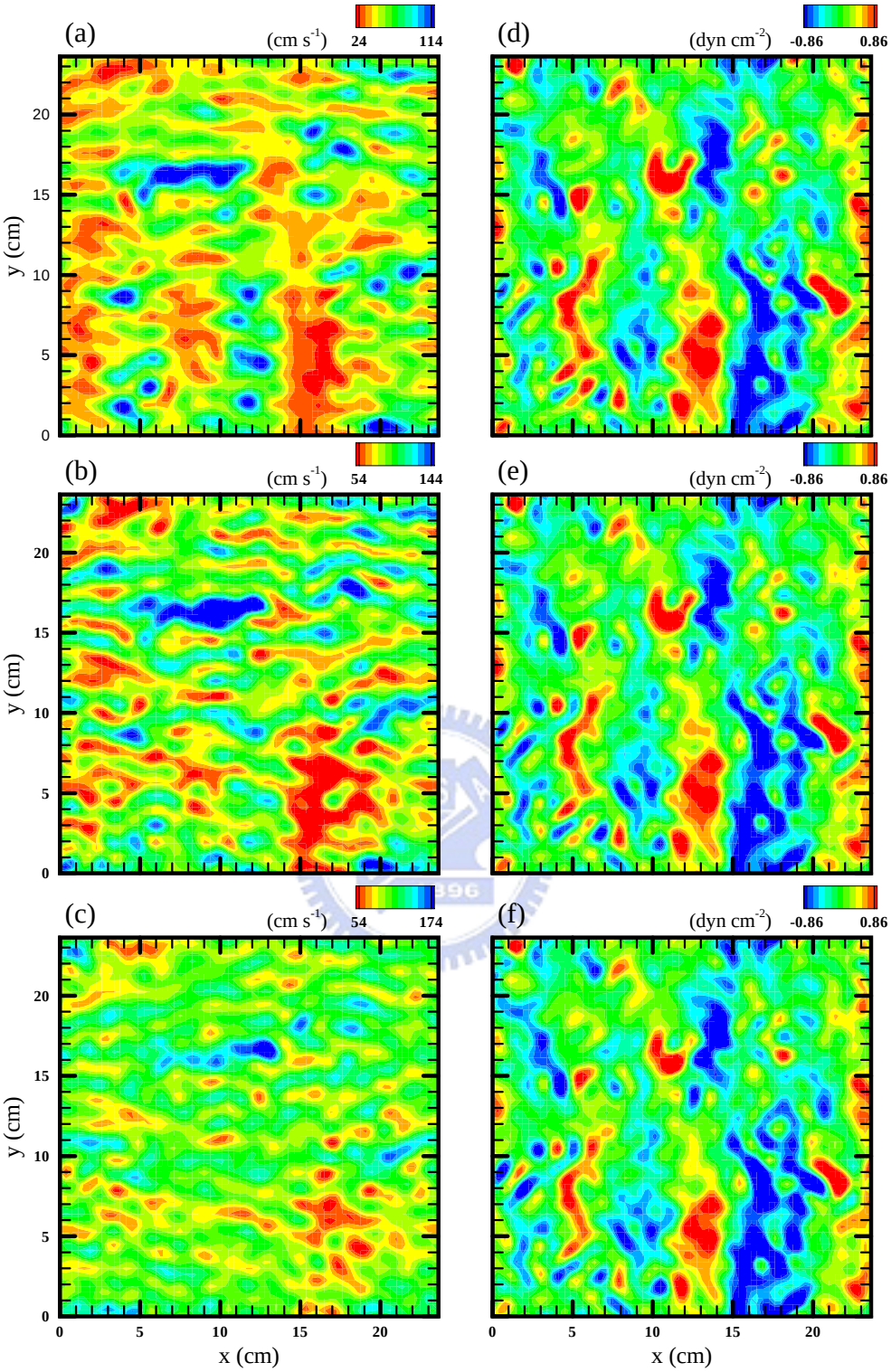

Figure 8. Snapshots of the instantaneous streamwise velocity (left panels) and pressure fluctuations (right panels) of the air flow in (x, y) – planes at t=64s at three different heights. The upper panels are within the viscous sublayer $z = 0.045\,\text{cm}$, middle panels are in the matched layer $z = 0.23\,\text{cm}$, and lower panels are in the inertial sublayer $z = 0.37\,\text{cm}$.

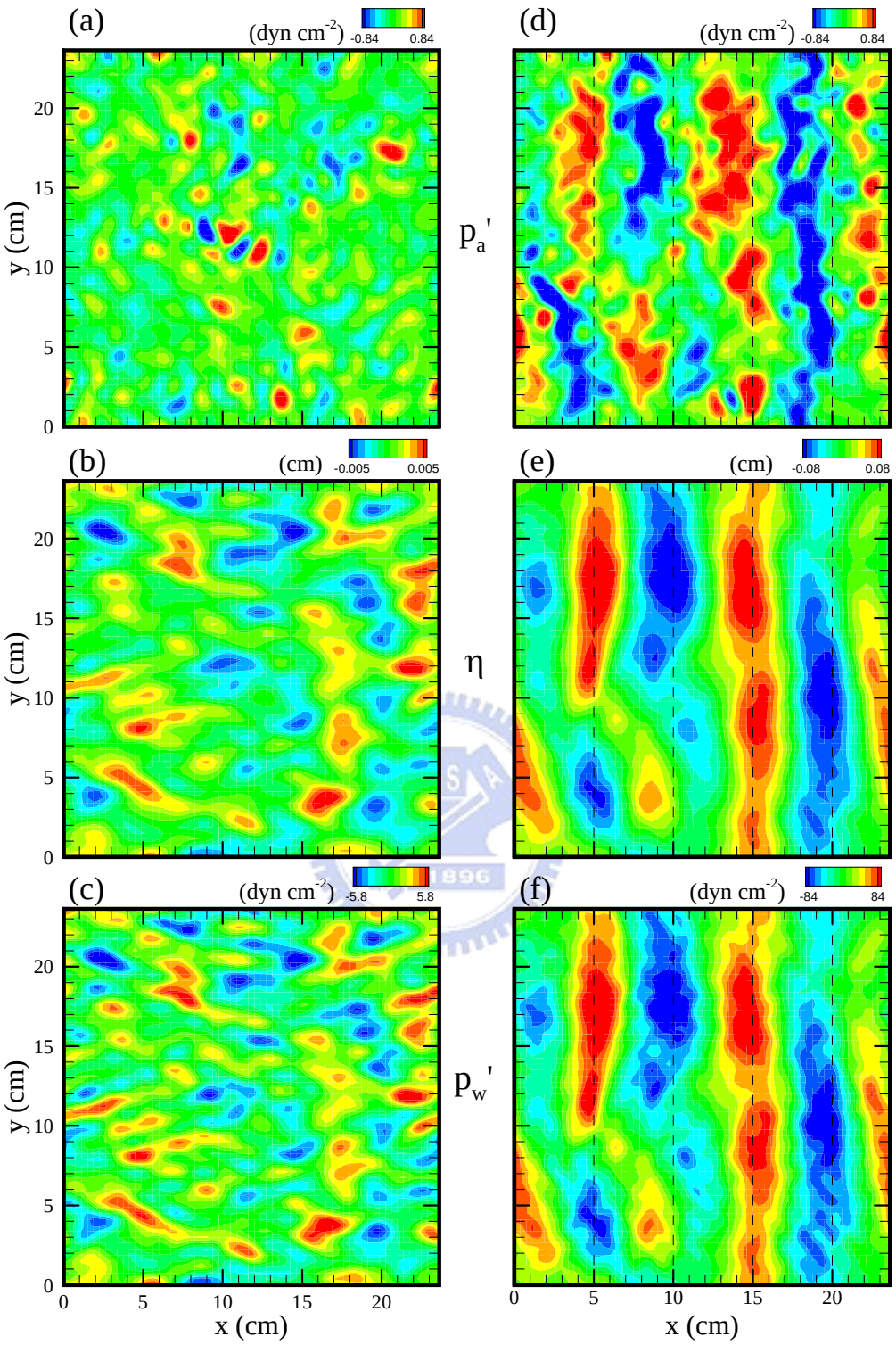

Figure 9. Snapshots of the instantaneous pressure fluctuations of the air p_a' (*a*, *d*) and water p_w' (*c*, *f*), and wave height η (*b*, *e*) on the interface at time $t = 16\,\mathrm{s}$ (left column) and $t = 66\,\mathrm{s}$ (right column).

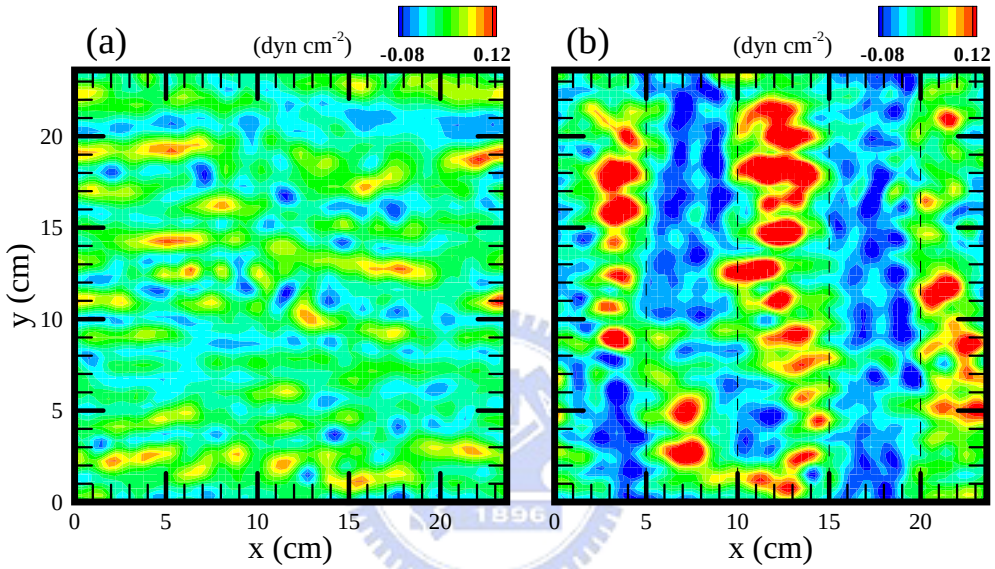

Figure 10. Snapshots of the instantaneous shear stress fluctuations τ_s' at the interface at time $t = 16\,\mathrm{s}$ (*a*) and $t = 66\,\mathrm{s}$ (*b*).

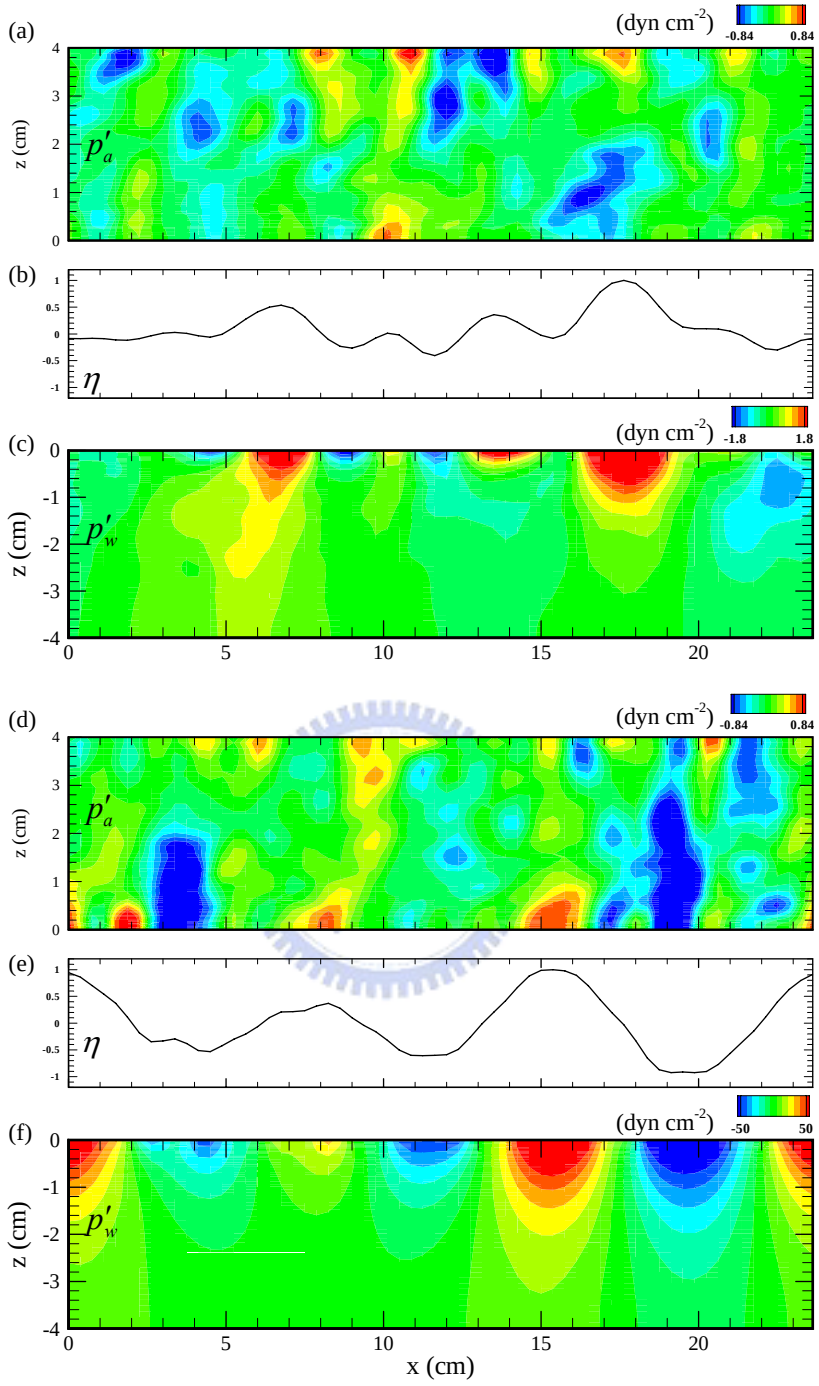

Figure 11. Snapshots of instantaneous pressure fluctuations in the air p'_a and water p'_w in an (x,z) – plane and the associated surface wave height η at time $t=16\,\mathrm{s}$ (figures *a-c*) and $t=66\,\mathrm{s}$ (figures *d-f*). The cross section is located at $y=7.5\,\mathrm{cm}$ in figure 9. η is normalized by its maximum value at this time.

Chapter IV

Characteristics of the surface waves

Figure 12 shows the wavenumber spectra of surface elevation at $t = 2.6$, 16 and 64 s. At the beginning of the simulation ($t = 2.6$ s) when the surface wave height is randomly distributed (figure 5*a*), the spectrum shows no significant energy in the low wavenumber range (figure 12*a*). As waves begin to form at $t = 16$ s (figure 5*b*), the wave energy is more or less evenly distributed at certain selected wave components (figure 12*b*). When waves become strong at $t = 64$ s (figure 5*c*), wave energy is concentrated in a few small-wavenumber components (figure 12*c*). Table 1 lists the five largest energy-containing components at early ($t \sim 15$ s) and late ($t \sim 68$ s) stages. At early time, the fraction of energy in each component is low and rather evenly distributed. At a later stage, about 80 % of wave energy is possessed by three wave components. These fastest growing waves are $(k_x, k_y) = (0.78, 0.)$, (0.52, 0.) and $(0.78, 0.26)$ cm^{-1}. Their associated wavelengths are in the range of 8 to 12 cm, close to those found by Kahama & Donelan (1988) in their laboratory experiment. The wavenumber-frequency spectrum of the surface wave elevations are plotted in figure 13 for the time interval $t = 66 \sim 66.5$ s. It shows that the frequency of the most energetic wave component $(k_x, k_y) = (0.78, 0.)$ cm^{-1} is 36.9 s^{-1} which agrees with the linear dispersion relation for a propagating gravity wave (dashed line in figure 13).

Theoretical study (Massel 1996) predicts this component a wind-induced gravity wave for wave frequency within the range of $0.19 < \sigma < 85$ s^{-1}. Experimental results from Veron & Melville (2001) also show that the first detectable wind-induced gravity wave is at a frequency of about 88 s^{-1}, and most of the detectable waves are located at a frequency of 25 s^{-1}. Thus, we believe the waves generated from our simulation are wind-induced gravity waves.

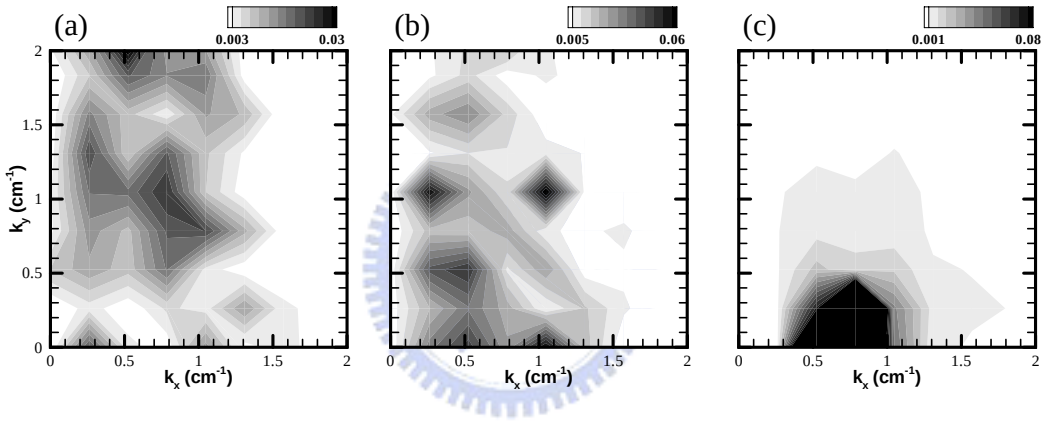

Figure 12. Wavenumber spectra of surface wave height $\hat{\eta}\left(k_x, k_y\right)$ (normalized by its total energy) at time $t = 0.5\,\mathrm{s}$ (*a*), $t = 16\,\mathrm{s}$ (*b*) and $t = 64\,\mathrm{s}$ (*c*). Note that the maximum contour level in (*c*) is higher than that in (*a*) and (*b*).

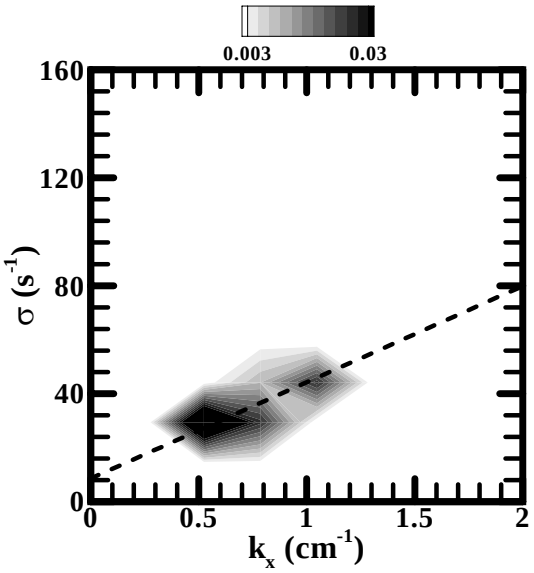

Figure 13. Wavenumber-frequency spectrum of the surface wave height $\hat{\eta}(k_x, \sigma)$ (normalized by its total energy) at time interval $t = 66 \sim 66.5\,\mathrm{s}$ for $k_y = 0$. The dashed line represents the linear dispersion relation $\sigma / k_x = U_s + \sqrt{g / k_x}$ where $U_s = 12$ cm s^{-1} is the mean surface current.

	Wave number $\kappa = (k_x, k_y)$ (cm^{-1})	$\Phi(\eta)/<\eta^2>^{1/2}$
$t \sim 15$ s	(0.26, 1.)	7.1 %
	(1., 1.)	5.6 %
	(1., 0.)	5.3 %
	(0.52, 0.)	4.5 %
	(0.52, 0.52)	4.1 %
t ~ 68 s	(0.78, 0.)	32 %
	(0.52, 0.)	24 %
	(0.78, 0.26)	21 %
	(0.52, 0.26)	7.6 %
	(1., 0.26)	5 %

Table 1 Dominate waves and the percentage of each wave energy at early (t~15s) and late (t~68 s) stages for the control case. Note that the dominate waves at these two stages are different.

Chapter V

Wave effect on flow fields

V.1 Wave effect on mean velocity profiles

Surface waves at the air-sea interface have significant effects on the mean velocity profiles of air and water flows (Sullivan *el al*., 2000, Cheung & Street, 1988 and Howe *et al.*, 1982). To examine the wave effect on the mean velocity profiles, we compare the air and water mean velocity profiles in our simulation with the two-layer velocity profile of a wall turbulent boundary layer

$$U^+ = z^+, \tag{5.1}$$

within the viscous sublayer, and

$$U^+ = \frac{1}{\kappa}\ln z^+ + b \equiv \frac{1}{\kappa}\ln\frac{z^+}{z_0^+}, \tag{5.2}$$

in the inertial layer, where κ is the von Karman constant, b is a constant related to the surface roughness length z_0^+, and $z_0^+ = e^{-\kappa b}$. The non-dimensional wall coordinate z^+ and velocity U^+ are defined as $z_a u_a^* / \nu_a$ and $(U_a - U_s)/u_a^*$ in the air and $-z_w u_w^* / \nu_w$ and $(U_s - U_w)/u_w^*$ in the water, respectively. U_s is the mean velocity at the interface, and U_a and U_w are the mean velocities in the air and in the water, respectively.

We compute the mean velocities by averaging the flow field in horizontal planes at each time, and plot the time variation of these mean velocities in figures 14(*a*) and 14(*b*), along with the theoretical profiles. Figure 14(*a*) shows that the simulated mean velocity profiles in the air compare well with the theoretical two-layer velocity profile. When surface waves are small ($t < 50\,\mathrm{s}$), the mean velocity profiles fit the same linear-logarithmic profile.

But, when surface waves become significant ($t > 50\,\mathrm{s}$), wave motions change the mean velocity profiles, a systematic downward shift with time. This downward shift in the air velocity profile is equivalent to an increase in surface roughness z_0^+ (figure 16*f*), as described in Sullivan *et al.* (2004), implying the enhancement of surface drag due to waves. The surface roughness z_0^+ is nearly constant ~ 0.3 when $t < 50\,\mathrm{s}$ and increases to about 0.95 when $t \sim 70\,\mathrm{s}$. The associated von Karman constant used to fit the logarithmic profile is about 0.33 at all time. Figure 14(*b*) shows the simulated mean velocity profiles and their associated two-layer velocity profiles in the water. Not all profiles show the logarithmic distribution and the von Karman constant κ is changing with time, $0.22 < \kappa < 0.36$ when $t < 24$ s and $0.36 < \kappa < 0.44$ when $t > 24$ s. (At t=3 s, the flow in the water may be too viscous as the mean wind profile is rather linear throughout.) The mean velocity profiles do not undergo a systematic downward shift with time as in the air.

V.2 Wave effect on and turbulence intensities

The wave effect on the turbulent velocity variances is also different in air and water. Figure 15 shows the turbulent velocity variances at two stages: $t = 16\,\mathrm{s}$ when turbulence dominates (figure 15*a* and 15*b*) and $t = 64\,\mathrm{s}$ when waves dominate (figures 15*c* and 15*d*). In the air, the vertical distributions of the velocity variances (normalized by the surface friction velocity) $\langle u_i'^2 \rangle(z) \big/ \left(u_a^*\right)^2$ are in close agreement with wall-bounded shear turbulent flows (Kim *et al.* 1987, Aydin & Leutheusser 1991, Papavassiliou & Hanratty 1997 and Sullivan *et al.* 2000). There is no significant change between turbulence and wave-dominated stages. In the water, our profiles at $t = 16\,\mathrm{s}$ agree with the stress-driven turbulent flow simulated by Tsai *et al.* (2005). However, at the stage when waves become significant, the velocity variances in the water are strongly affected by waves, particularly the w component. The horizontal-velocity variances near the interface also increase significantly due to waves. Such an enhancement in the near surface turbulent velocity variances is attributed to the orbital motions of the generated surface waves.

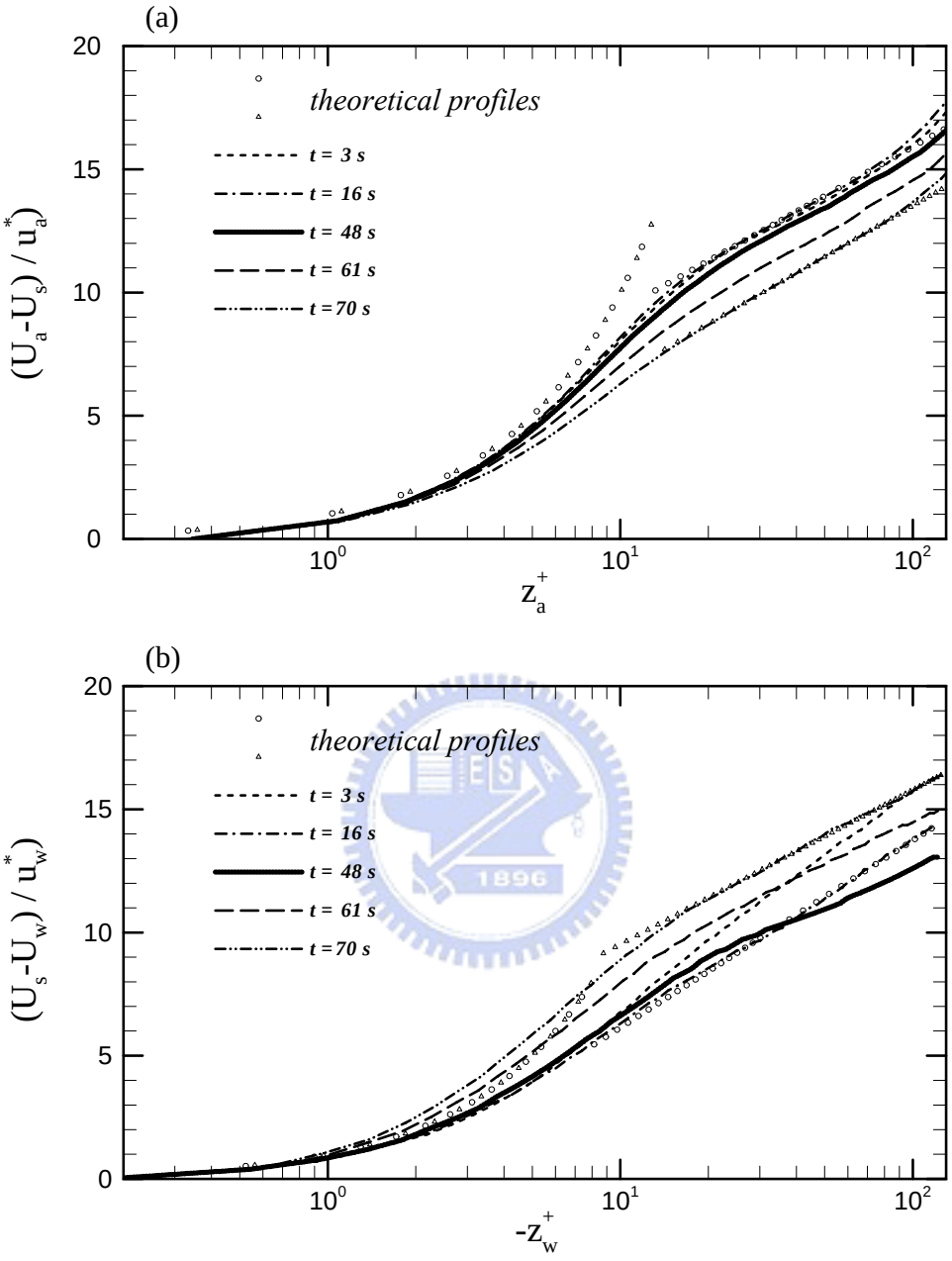

Figure 14. Mean profiles of the streamwise velocity of the air (*a*) and water (*b*). The circular and delta symbols denote the matched linear-logarithmic profiles at $t = 16\,\mathrm{s}$ and $t = 70\,\mathrm{s}$, respectively. The log-law constants used to collapse the profiles $\left(\kappa, z_0^+\right)$ are (0.34, 0.31) and (0.33, 0.84) in the air and $\left(\kappa, z_0^+\right)$ are (0.3, 1.55) and (0.37, 0.3) in the water at time $t = 16\,\mathrm{s}$ and $t = 70\,\mathrm{s}$, respectively.

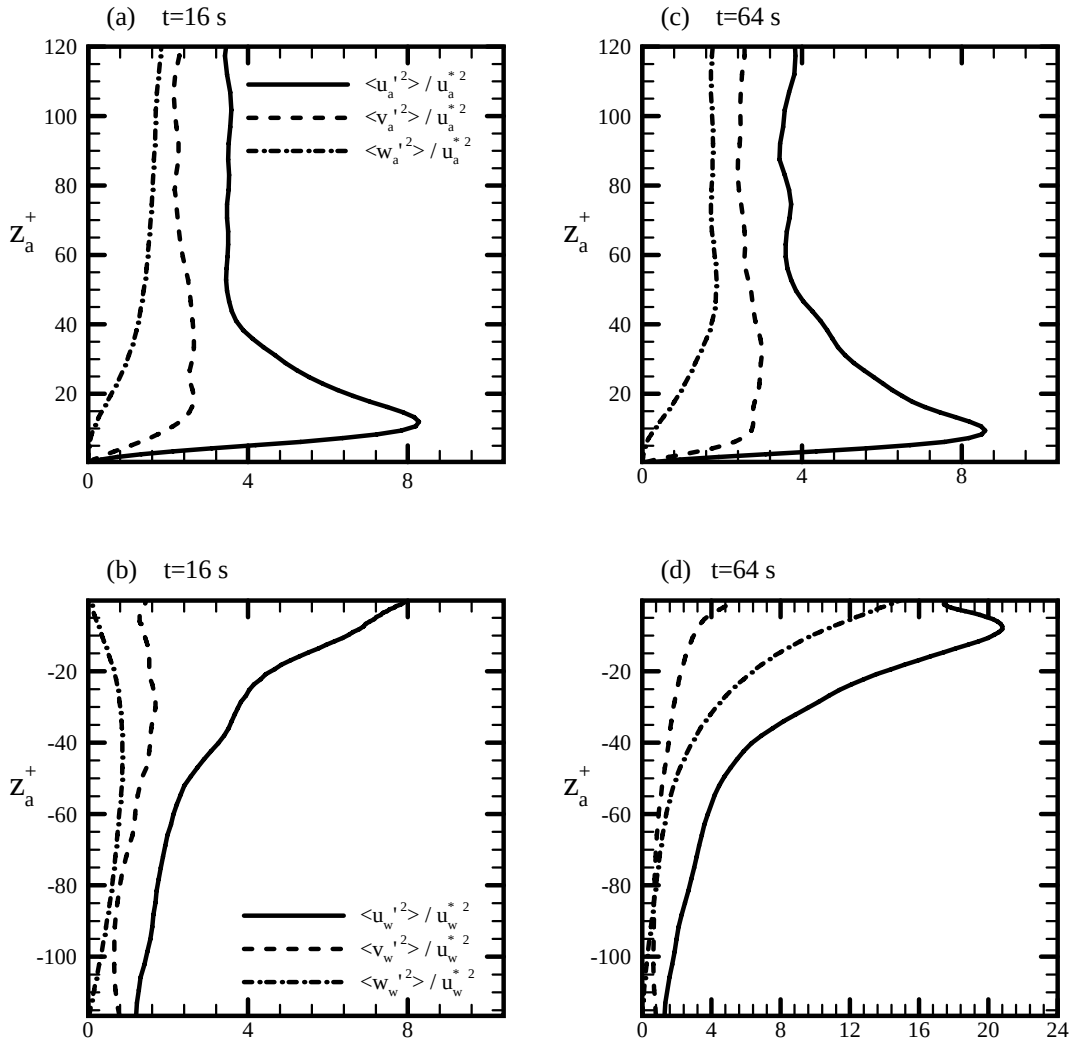

Figure 15. Vertical distributions of the normalized turbulent velocity variances of the air (upper panels) and of the water (lower panels) at early ($t = 16\,\mathrm{s}$) and later ($t = 64\,\mathrm{s}$) stages.

Chapter VI

Wave growth types

Previous theoretical studies suggest that wave growth processes can be separated into linear and exponential growth stages and that the forcing mechanisms may involve either turbulence-induced or wave-induced pressure and stress fluctuations. The consensus is that in the linear growth stage, the wave-induced effects are ineffective since wave motions are weak and thus turbulence plays a major role in generating waves. In the exponential growth stage, wave-induced fluctuations of pressure and stress dominate and result in a feedback mechanism to grow waves quickly. In this study, we examine the wave growth processes in our simulated flow by classifying the simulation into linear and exponential wave-growth stages using four features as follows.

First, the behaviour of pressure and shear stress fluctuations in the air is different at early and later stages as described in section 3.2; they are turbulence dominated at early stage and wave dominated at later stage. Second, the time evolution of the root-mean-square of surface wave height $\langle \eta^2 \rangle^{1/2}$ (figure 16*a*) clearly shows slow growth before $t \sim 40\,\mathrm{s}$ and fast growth after $t \sim 40\,\mathrm{s}$. Other statistical quantities, such as $\langle p_a'^2 \rangle^{1/2}$, the form drag D_p, the mean surface current U_s, the root-mean-square of the interfacial shear-stress fluctuations $\langle \tau_s'^2 \rangle^{1/2}$ and the surface roughness z_0^+ (shown in figures 16*b* – *f*) also behave differently during early and late stages of the wave growth. They are nearly constant before $t \sim 40\,\mathrm{s}$ and then increase sharply with time. Third, the individual wave components of the fastest growing modes given in Table 1 also reveal linear and exponential growth as shown in figure 17 where the time evolutions of the wave amplitudes of the five fastest-growing waves in linear coordinates for $t < 16\,\mathrm{s}$ are shown in figure 17(*a*), and the three fastest-growing waves in exponential coordinates for $40 < t < 68\,\mathrm{s}$ in figure 17(*b*). They clearly reveal trends of linear

and exponential growth for each wave mode at the early and later stages, respectively. Fourth, each wave component of the form stress also shows different behaviour at the early and later stages of wave growth. Here we define the dimensional form stress per unit area, D_p, of each wave component as

$$D_p = \frac{1}{L_x L_y} \int_0^{L_y} \int_0^{L_x} p_a' \left(\frac{\partial \eta}{\partial x} + \frac{\partial \eta}{\partial y} \right) dx\, dy\,. \tag{6.1}$$

Again we plot the time evolution of D_p of the five largest waves in linear coordinates for $t < 16\,\mathrm{s}$ in figure 18(*a*) and the largest three waves in exponential coordinates during $40 < t < 68\,\mathrm{s}$ in figure 18(*b*). The form stress is nearly zero when $t < 16\,\mathrm{s}$ but increases exponentially with time when $t > 40\,\mathrm{s}$. Because the form stress oscillates rapidly in the transition regime between 40 s and 50 s, we choose $0 < t < 16\,\mathrm{s}$ as the linear growth stage and $50 < t < 70\,\mathrm{s}$ as the exponential growth stage.

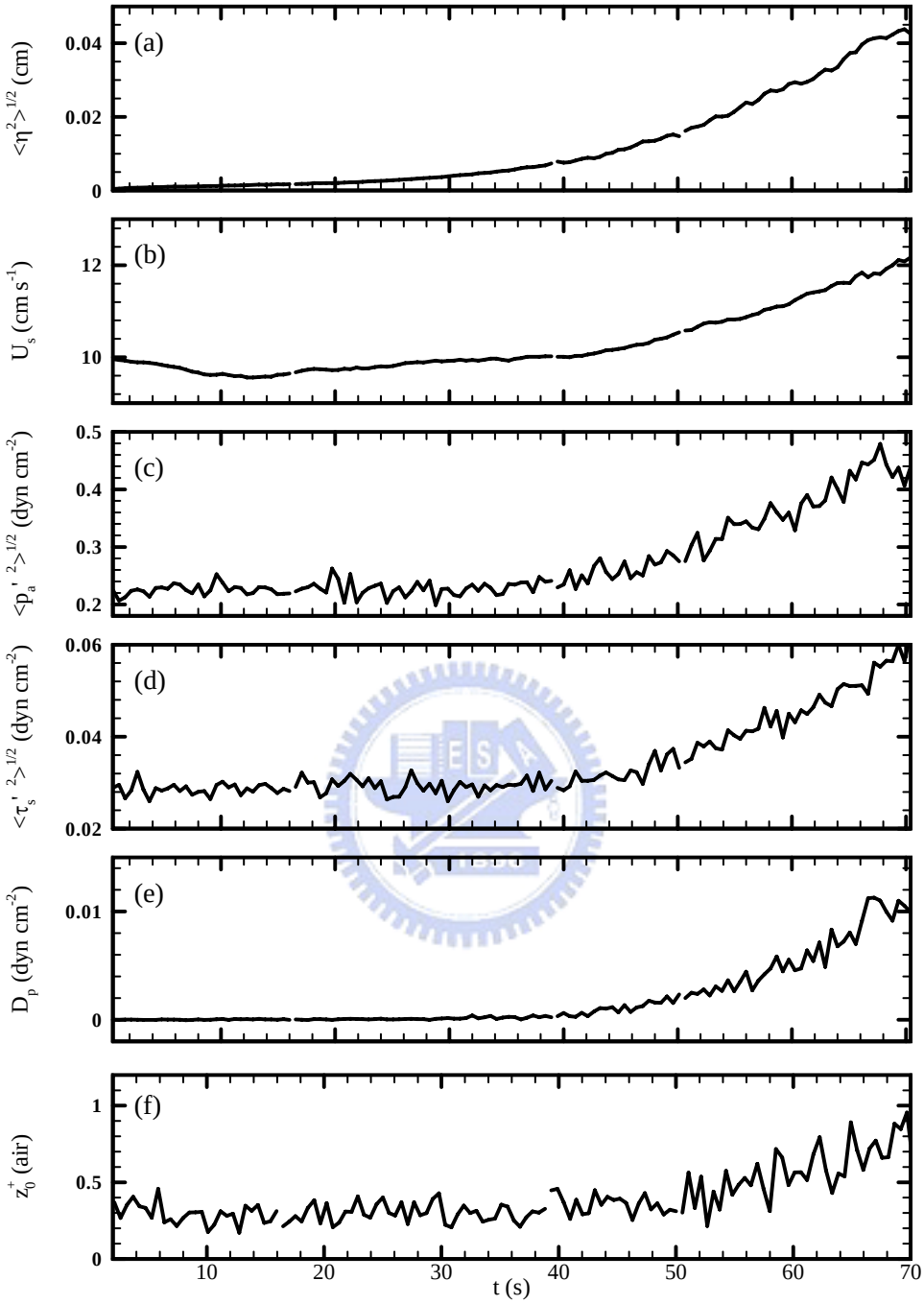

Figure 16. Time evolution of interfacial parameters: (*a*) root-mean-square of the surface wave height $\langle \eta^2 \rangle^{1/2}$, (*b*) root-mean-square of pressure fluctuations $\langle p_a'^2 \rangle^{1/2}$, (*c*) form stress D_p, (*d*) mean surface current U_s, (*e*) root-mean-square of shear stress fluctuations $\langle \tau_s'^2 \rangle^{1/2}$ and (*f*) surface roughness length z_0^+ of the air.

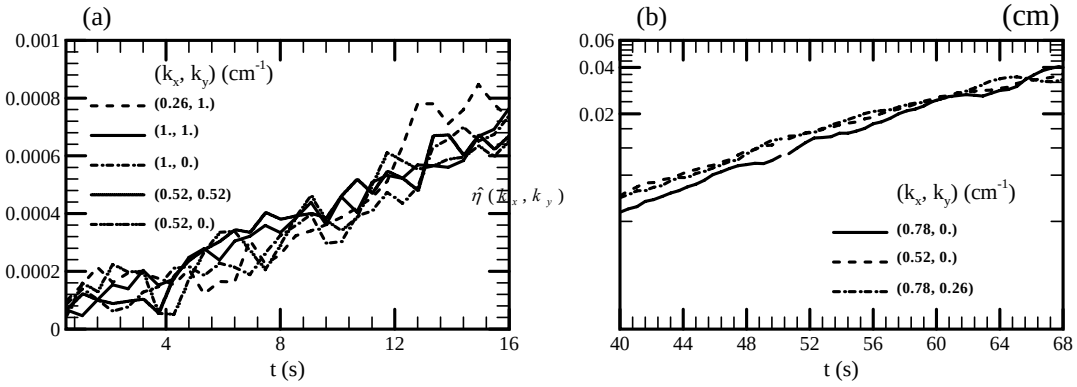

Figure 17. Time evolutions of wave amplitudes of the five fastest growth waves at early stage (*a*), and the three fastest growth waves at late stage (*b*). Note that we use a linear coordinate for (a) but an exponential coordinate for (b).

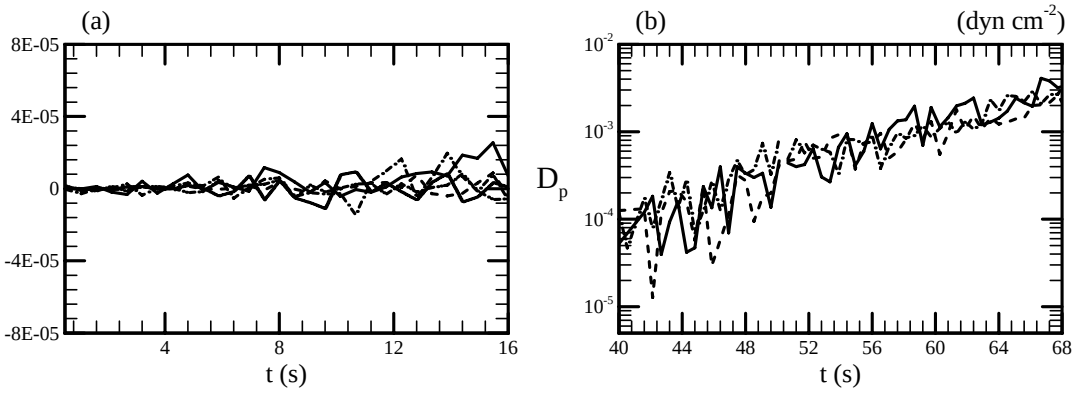

Figure 18. Time evolution of the form stress D_p for the same wave modes as those shown in figure 17.

Chapter VII

Comparison with wind-wave generation theories and measurements

VII.1 Linear growth stage

Phillips (1957) proposed a theoretical model for wave generation and argued that the turbulence-induced pressure fluctuations in the air are responsible for the birth and early growth of waves. His theoretical model predicts that the wave growth of each wavenumber k depends on the time scale of the pressure fluctuations in air of the same wavenumber k.

For the pressure field of the air varies little from its value at the initial instant (pressure components remain correlated with the one at the initial instant), in which case we will be able to argue as though the pressure field were being convected over the water as a rigid body, Phillips' (1957) derivation leads to a resonance mechanism that explains the initialization of wave growth. The resonance mechanism occurs when the convection speed of the fluctuating pressure coincides with the phase velocity of surface waves at the same wavenumber, i.e. $U_c(\kappa) = c(\kappa)/\cos\alpha$, where $U_c(\kappa)$ is the convection speed of the fluctuating pressure in the wind direction, and α is the angle of wave propagation relative to wind direction. From the flow field at the early stage of our simulation ($t < 16\,\mathrm{s}$), we found that for each wavenumber, the convection speed of the pressure fluctuations in the air is always larger than the phase speed of the surface wave. In other words, no resonance mode is found in our simulations. The lack of a resonance mode is likely due to our flow condition is unable to fulfill Phillips' assumption that the pressure is assumed to be time-invariant.

For the time period much larger than the time scale of pressure fluctuations, Phillips' derivation considers the time development of turbulence pressure fluctuations, and that leads to the following prediction for the linear growth of the wave spectrum $\Phi(\kappa,t)$

$$\Phi(\kappa,t) \sim \frac{k^2\,\Pi(\kappa)\Theta(\kappa)}{2\sqrt{2}\rho_w^2\sigma^2}t\,, \tag{7.1}$$

where $\Pi(\kappa)$ is the pressure spectrum, σ is the wave frequency, and $\Theta(\kappa)$ is the development time scale in turbulence pressure fluctuations. For the definition of $\Theta(\kappa)$, readers are referred to equation (4.2.5) in Phillips (1977). Application of (7.1) is however hindered by the factor $\Theta(\kappa)$, which is difficult to compute from a simulated flow field. Thus we use a simplified version of (7.1) proposed by Phillips (1957)

$$\Phi(\kappa,t) \sim \frac{\Pi(\kappa)}{2\sqrt{2}\rho_w^2 g U_c(\kappa)}t\,. \tag{7.2}$$

The simplification from (7.1) to (7.2) is obtained by (a) using the gravity-wave dispersion relation with no mean surface current at the interface, $\sigma^2 = gk$ and (b) assuming $U_c(\kappa)$ is greater than $c(\kappa)/\cos\alpha$ by a factor of 3-4, then $\Theta(\kappa) \sim 1/kU_c(\kappa)$. Transforming to physical space, (7.2) becomes

$$<\xi^2> \sim \frac{<p_a'^2>}{2\sqrt{2}\rho_w^2 g U_c}t\,. \tag{7.3}$$

Equation (7.2) has limitations. It is inadequate for waves with low wavenumber at high wind speed (said a wind speed larger than $10\,\mathrm{m\,sec^{-1}}$) and for waves with high wavenumber at low wind speed (said a wind speed smaller than $1\,\mathrm{m\,sec^{-1}}$). This is due to the different behaviour of $\Theta(\kappa)$ at high and low wind speeds and the relation between $\Theta(\kappa)$ and $\kappa\,\Pi(\kappa)$. For a detailed interpretation, readers are referred to Phillips (1957, pages 437—440). In our numerical experiments, the wind is mild and the generated surface waves are mostly high wavenumber. So it may not be proper to compare our simulation with equation (7.2).

For the application of (7.3), Phillips' (1957) proposed the following relation between air friction velocity and convection speed

$$U_c \sim 18\, u_a^*, \tag{7.4}$$

based on field measurements. By using this relation, we obtain a convection speed U_c of about $162\,\mathrm{cm\,s^{-1}}$ (where $u_a^* \sim 9\,\mathrm{cm\,s^{-1}}$) which is close to the mean wind speed in the simulated logarithmic layer where $U_a \sim 170 \pm 20\,\mathrm{cm\,s^{-1}}$. Figure 19*a* compares the mean square surface wave height from our simulation $\langle \eta^2 \rangle$ and the prediction $\langle \xi^2 \rangle$ from (7.3). Our simulated growth rate is larger than the theoretical prediction by a factor of about 1.5. The other three simulations shown in figures 19(*b*-*d*) will be described in section 8.

As mentioned previously, wind energy can be transferred into waves by pressure and shear stress fluctuations. Figures 16(*c*) and 16(*d*) show that in the linear growth stage the root-mean-square shear stress fluctuations is about one-tenth of the root-mean-square pressure fluctuations where $\langle p_a'^2 \rangle^{1/2}$ is about $0.22\,\mathrm{dyn\,cm^{-2}}$ (figure 16*c*) and $\langle \tau_s'^2 \rangle^{1/2}$ is about $0.029\,\mathrm{dyn\,cm^{-2}}$ (figure 16*d*). Their ratio is close to the value measured in laboratory boundary layers (Phillips, 1977). Therefore, the contribution to wave growth from $\langle \tau_s'^2 \rangle$ is about 17% of $\langle p_a'^2 \rangle$. Furthermore, measurements from atmospheric and laboratory boundary layers (Elliott 1972*a*,*b*) show that $\langle p_a'^2 \rangle^{1/2}$ is about 2.6 times larger than the mean wind stress τ_s (see figures 16*c* and 3). Our simulation shows that the mean wind stress is about 0.085 dyn cm^{-2} (figure 3) during $t < 20\,\mathrm{s}$ and thus our $\langle p_a'^2 \rangle^{1/2}$ is also about 2.6 times larger than the mean wind stress.

VII.2 Exponential growth stage

Many theories have been proposed to explain the exponential growth of wind generated surface waves. By examining the various processes that generate the asymmetric pressure perturbation at the surface, Belcher & Hunt (1993) show that the term induced by the thickening of the perturbed boundary layer on the leeside of the wave crest, which is called the non-separated sheltering effect, dominates. Furthermore, they relate the asymmetric effects to the drag force on the wave. When the asymmetric effect grows with time, it also

increases the form stress on waves. This way, the form stress can play an important role in the exponential wave growth stage.

Here we calculate the growth rate of our simulated waves and compare it to measurements synthesized by Plant (1982) and to theoretical (Belcher & Hunt 1993; Li 1995) and numerical studies (Sullivan & McWilliams 2002). The wave growth rate is defined as

$$\beta^* = \frac{2}{a}\frac{da}{dt} = \frac{1}{E}\frac{dE}{dt}, \tag{7.5}$$

where β^* is dimensional wave growth rate, a is wave amplitude and $E = 0.5\rho_w a^2 c^2 k$ is wave energy density. Since the form stress dominates the contribution of energy input from the perturbed air flow to surface waves, the dimensionless wave growth rate β (where $\beta = \beta^* / \sigma$ and σ is wave frequency) computed from the right hand side of equation (7.5) can also be expressed as (Li 1995)

$$\beta = \frac{1}{\sigma E}\frac{dE}{dt} = \frac{2}{\rho_w}\frac{D_p}{(ak)^2}\left(\frac{1}{c}\right)^2, \tag{7.4}$$

where the relation between the rate of change of the wave energy, dE/dt, and the form stress, D_p, is given as $dE/dt = cD_p$. We compute the growth rates from the above two relations and examine the contribution of form stress to wave growth. The one computed directly from wave amplitude is used to verify the contribution of form stress on wave growth. Figure 20(*a*) shows the time averaging (t=56~70s) of the growth rates of the three fast-growing wave components from our simulation. The growth rates calculated directly from the wave amplitude and from the form stress are similar to each other. For some wave modes the rates are close to the measurements synthesized by Plant (1982) and the simulation results from Li (1995) and Sullivan & McWilliams (2002) but others are 2-3 times larger than the measurements and theoretical predictions. The other three simulations shown in figures 20(*b-d*) are described in section 8.

The consistency of the growth rates calculated from wave amplitude and form stress supports Belcher & Hunt's (1993) argument that the form stress dominates the contribution of energy input from air to waves at the exponential wave growth stage.

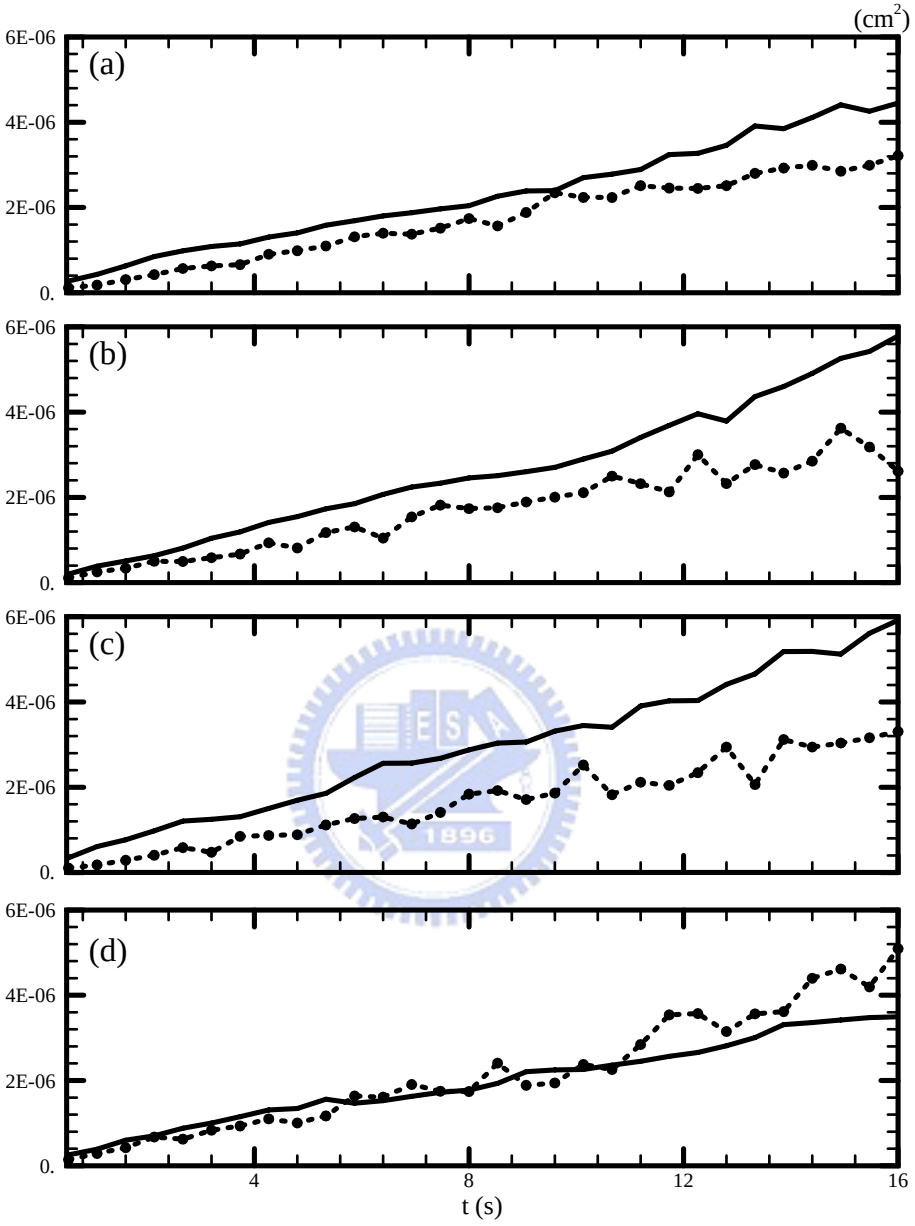

Figure 19. The comparison of the mean square surface wave height between our numerical results $\langle \eta^2 \rangle$ (solid lines) from four simulations and the theoretical predictions $\langle \xi^2 \rangle$ (dashed-dotted lines) of Phillips (1957). The four simulations are : (*a*) the control run with the height of the air domain h = 4 cm, (*b*) the run with no initial turbulence in the water, (*c*) the run with no surface tension and (*d*) the run with the height of the air domain h = 8 cm. For the theoretical curves, $U_c = 18\, u_a^*$ is used.

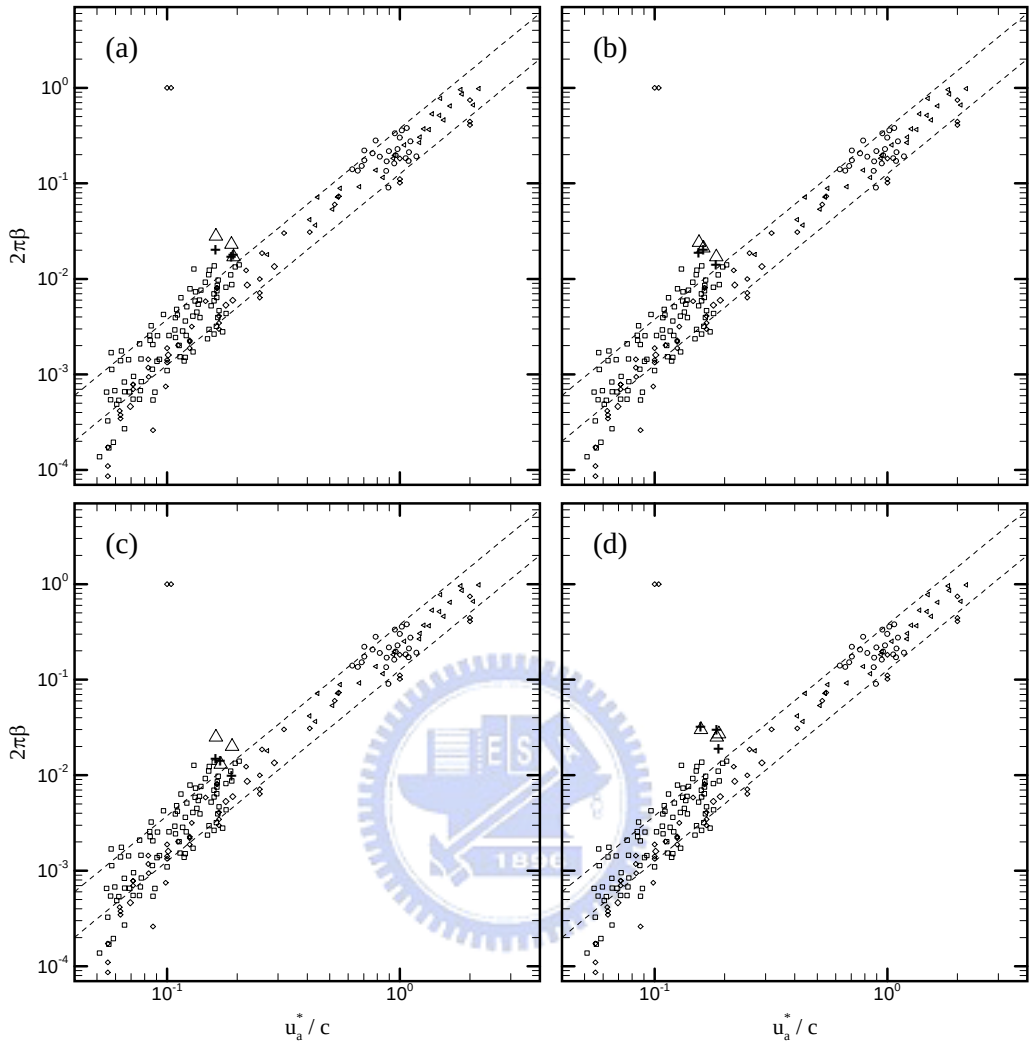

Figure 20. Wave growth rate as a function of inverse wave age. Small symbols are results from the measurements (synthesized by Plant, 1982) and the simulation results (Li, 1995; Sullivan & McWilliams, 2002) as published in Sullivan & McWilliams (2002). The dashed lines are the empirical formula $\beta = (0.04 \pm 0.02)(u_*/c)^2$ proposed by Plant (1982) The cross and large triangle symbols are our results calculated from the growth of wave amplitude (7.3) and from the form stress (7.4), respectively, for the three fast-growing wave components. The three fast-growing wave components are $(k_x, k_y) = (0.78, 0.)$, $(0.52, 0.)$ and $(0.78, 0.26)$ cm^{-1} for the control simulation (*a*), $(0.52, 0.)$, $(0.78, 0.26)$ and $(0.52, 0.26)\,\mathrm{cm}^{-1}$ for the simulation with no initial turbulence in the water (*b*), $(0.78, 0.)$, $(0.52, 0.26)$ and $(0.52, 0.)\,\mathrm{cm}^{-1}$ for the simulation with no surface tension (*c*), and $(0.52, 0.)$, $(0.78, 0.)$ and $(0.78, 0.26)\,\mathrm{cm}^{-1}$ for the simulation with larger air domain (*d*).

Chapter VIII

Sensitivity tests

VIII.1 The effects of turbulence in the water

To study other possible mechanisms that may influence the simulated wave growth processes, we perform three sensitivity tests to examine the effects of turbulence in the water, surface tension and the computational domain height above the water surface.

Our first sensitivity test was motivated by Teixeira & Belcher's (2006) study. Teixeira & Belcher developed an analytical model to test the influence of turbulence in the air and in the water, separately, on surface wave growth. They suggested that turbulence in the water might play an important role, more than that suggested by Phillips (1957). To test their finding, we set up a simulation that consists of no turbulence in the water at the beginning of the simulation (that is, at our initialization procedure described in section 2.5 we do not allow for turbulence in the water to spin up before the interface starts to deform). Figures 21(*c*,*d*) compare the wave energy spectrum of the surface wave height at time $t = 16\,\mathrm{s}$ and $t = 64\,\mathrm{s}$ between the cases with and without turbulence in the water at the initial time of wave growth. Similar to the simulation with turbulence in the water (i.e., the control case) the case without turbulence in the water shows a spread of wave energy in wavenumber space at the early stage ($t = 16\,\mathrm{s}$), but then energy begins to be concentrated to just a few dominate wave components that have similar wavelengths as the control case at the exponential growth stage ($t = 64\,\mathrm{s}$). We also compare the growth rates from this sensitivity test with theoretical predictions by Phillips (1957). In the linear growth stage, the magnitudes of the mean square surface wave height are similar between the simulations with and without turbulence in the water (comparing figure 19*a* and 19*b*). Figure 20(*b*) indicates that turbulence in the water

also has no significant effect on the wave growth in the exponential growth stage.

VIII.2 The effects of surface tension

In the second sensitivity test, the surface tension in the interfacial boundary condition (2.9) is set to zero. The distributions of wave energy spectra (figures 21*e*,*f*) exhibit similar patterns as those from the previous two simulations with surface tension (figures 21*a*-*d*). The computed wave growth rates are slightly higher than the cases with surface tension at the linear growth stage (comparing figure 19*c* with figures 19*a*,*b*), but are similar to previous studies at the exponential growth stage (figure 20*c*). We conclude that surface tension has no significant impact on the initial wind-wave generation.

VIII.3 The effects of the computational domain of air

For the third sensitivity test, we double the height of the computational domain of air (while vertical resolution remains the same). The distribution of wave energy spectra shows similar patterns as the previous three cases (figures 21*g*,*h*). The linear wave growth rates of the larger-numerical domain simulation (figure 19*d*) are smaller than those of other three simulations (figures 19*a*-*c*), and are now closer to the theoretical predication of Phillips (1957). However, the wave growth rates from this simulation are a little larger than the other simulations and also larger than theoretical predictions at the exponential growth stage (figure 20*d*).

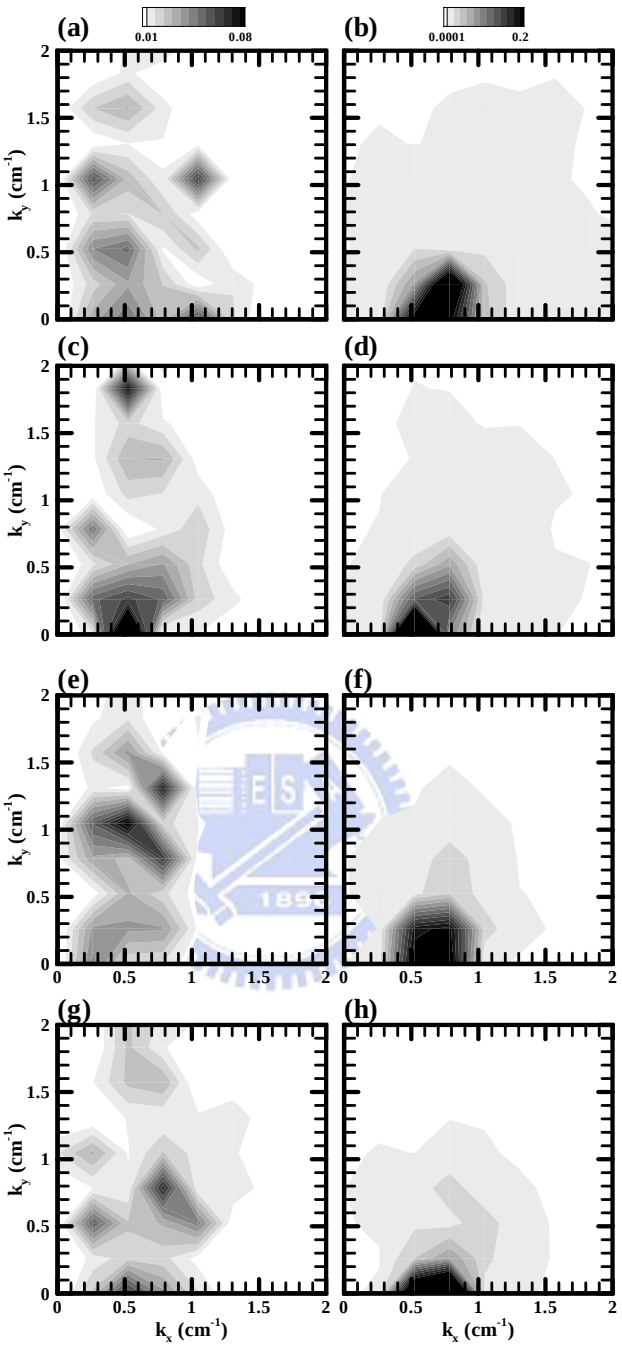

Figure 21. Wavenumber spectra of surface wave height $\hat{\eta}\left(k_x, k_y\right)$ (normalized by its total energy) at time $t = 16\,\mathrm{s}$ (left panels) and $t = 64\,\mathrm{s}$ (right panels) for the control case shown in (*a*, *b*), the simulation without generating turbulence in the water at the beginning of the simulation shown in (*c*, *d*), the simulation without surface tension at the interface in (*e*, *f*), and the simulation doubling the height of the computational domain of the air in (*g*, *h*).

Chapter IX

Conclusions

The initial wind-wave generation processes consist of linear and exponential growth stages as proposed by theoretical studies and supported by some laboratory and field measurements but these processes have never been studied by numerical simulation before. In this study we developed an air-water coupled model where the continuity of velocity and stress is satisfied at the interface so it can simulate the interaction of two fully developed turbulent layers (air and water) above and below the interface. The limitation of our coupled model is the linearization of the interfacial boundary conditions and hence the model is only applicable to small amplitude waves.

The characteristics of simulated waves are similar to field and laboratory observation at the initial stage of wind-wave generation. The wavelength of the dominate waves is about 8cm which is in the range of wind-induced gravity waves. The corresponding wave age $c/u_a^* \sim 5$ belongs to 'young sea' or 'slow moving waves'.

At the early stage of wave growth, the turbulent flow structures in the air (and in the water) remain similar to shear-driven turbulent flows over a flat surface (and under a flat free surface). At the later stage of our simulation, waves grow exponentially and the flow fields are strongly influenced by wave motions. The wave effects on the flow fields are summarized as follows. First, the streaky structure, which is a typical phenomenon of shear-driven turbulent flow, is interrupted by wave motions and the streamwise velocity field forms a pocket-like feature. Second, the flow field over the whole water domain is strongly affected by the waves at the later stage. This effect is evidenced from the iso-surface of vertical velocity, the vertical profiles of the mean velocity and turbulence intensity. Motions in the water are dominated by wavy features and the flow field in the water is nearly irrotational flow. This agrees with most

theoretical and experimental studies which assume water flow to be irrotational underneath the surface wave. Third, wave effects on the velocity field in the air are confined only in a thin viscous sublayer. The turbulence intensity of the air does not change significantly due to waves. Fourth, the pressure field in the air behaves differently at early and late stages. In the early stage, the pressure fluctuations of the air are mainly turbulent-induced and advect faster than the phase velocity of the waves. During the later stage, the air pressure fluctuations become wavelike throughout the turbulent layer and move along with the surface waves.

Similar to theoretical studies, our simulated waves can be separated into linear and exponential growth stages as distinguished by the following: (1) the behavior of pressure fluctuations in the air (which are considered to be the main factor that is available to initiate and support wave motion), (2) the simulated interfacial properties , (3) the growth trend, and (4) the magnitude of the form stress (which is considered to be the main contributor of energy transfer from wind to waves at the exponential growth stage).

Our growth rates are comparable to theoretical predictions, field and laboratory measurements, and other numerical simulations. In the linear growth stage, the theoretical prediction from Phillips' (1957) wind-wave generation mechanism is examined. Our wave growth rates are comparable to those theoretical predictions if we use an air domain that is deep enough. In the linear stage the simulations show that the contribution of shear stress fluctuations to the wave growth is about 17 % of pressure fluctuations contribution, which agrees with laboratory measurements. In the exponential growth stage, our wave growth is consistent with Belcher & Hunt's (1993) non-separated sheltering mechanism. However, the growth rates computed from our simulated waves are somewhat larger (by about a factor of 2) than those obtained from measurements (Plant 1982), simulations (Sullivan & McWilliams, 2002; Li, 1995) and Belcher & Hunt's (1993) theoretical prediction.

Appendix A

Numerical Method

I. Pressure Poisson Equations

To solve the Poisson equation (2.3), we transfer the pressure field and the source term into wave space and apply center-differencing scheme to calculate the vertical derivatives, which yields

$$\alpha_1 \, \hat{p}^{\ell}_{i,j,k} + \alpha_2 \, \hat{p}^{\ell}_{i,j,k} + D3^{\ell}_{k} \, \hat{p}^{\ell}_{i,j,k+1} + D2^{\ell}_{k} \, \hat{p}^{\ell}_{i,j,k} + D1^{\ell}_{k} \, \hat{p}^{\ell}_{i,j,k-1} = \hat{\mathrm{H}}^{\ell}, \qquad \text{(A.1)}$$

where coefficients α_1 and α_2 are produced from fast Fourier transform (FFT) ,and $D3^{\ell}_{k}$, $D2^{\ell}_{k}$ and $D1^{\ell}_{k}$ are coefficients from second-order finite-differencing schemes. For computational efficiency, we separated the coefficient matrix of equation (A.1) to two sub-matrices and used the interface from conditions (2.9) and (2.13). These two interfacial points can be treated as Dirichlet boundary conditions for each sub-domain. The sub-matrices became two tri-diagonal matrices and the computational time is greatly reduced.

II. Stretching Grid systems

In the vertical direction, the discretization grids are stretched with a finer resolution near the interface using the following transform functions

$$z^{a}_{k} = h^{a}\left[1 - \frac{\tanh(\alpha\varsigma_k)}{\tanh(\alpha)}\right] \qquad \text{in air,} \qquad \text{(A.2)}$$

and

$$z^{w}_{k} = -h^{w}\left[1 - \frac{\tanh(\alpha\varsigma_k)}{\tanh(\alpha)}\right] \qquad \text{in water,} \qquad \text{(A.3)}$$

where ς_k $(0 \le \varsigma_k \le 1)$ is uniformly distributed constants and $\alpha = 1.8417$ (Gavrilakis, 1992) is the degree of stretch.

Appendix B

Initialization

I. Analytical solution:
the mean velocity profile of the coupled air-water flow

The first step to initiate the simulation flow field is the assignment of mean velocity profile. We assign the mean velocity profile of the coupled air-water flow based on the analytical solution of laminar, transient flow (Choy & Reible 2000) at the time when the mean velocity at the interface reaches $8\,\mathrm{cm\,s^{-1}}$. The governing equations to describe this flow are

$$\frac{\partial U_a}{\partial t} = \nu_a \frac{\partial^2 U_a}{\partial z^2}, \tag{B.1}$$

$$\frac{\partial U_w}{\partial t} = \nu_w \frac{\partial^2 U_w}{\partial z^2}, \tag{B.2}$$

where boundary conditions are applied as

$$U_a(z=h,t) = U_0, \tag{B.3}$$

$$U_a(z=0,t) = U_w(z=0,t) \tag{B.4}$$

$$\mu_a \frac{\partial U_a(z=0,t)}{\partial z} = \mu_w \frac{\partial U_w(z=0,t)}{\partial t} \tag{B.5}$$

$$\frac{\partial U_w(z=-h,t)}{\partial z} = 0. \tag{B.6}$$

Generation solutions of U_a and U_w obtained by Choy & Reible (2000) are given as

$$U_a(z,t) = \sum_{n=1}^{\infty} \left\{ e^{-\beta_n^2 t} \frac{1}{N(\beta_n)} \psi_a(\beta_n, z) I_0(\beta_n) \right\}, \tag{B.7}$$

$$U_w(z,t) = \sum_{n=1}^{\infty} \left\{ e^{-\beta_n^2 t} \frac{1}{N(\beta_n)} \psi_w(\beta_n, z) I_0(\beta_n) \right\}, \tag{B.8}$$

where

$$N(\beta_n) = \rho_w \int [\psi_w(\beta_n, z')]^2 dz' + \rho_a \int [\psi_a(\beta_n, z')]^2 dz', \tag{B.9}$$

$$I_0(\beta_n) = \rho_w \int_{-h}^{0} \psi_w(\beta_n, z') C_0(z') dz' + \rho_a \int_0^h \psi_a(\beta_n, z') C_0(z') dz', \tag{B.10}$$

and $C_0(z)$ is the initial condition. ψ_a and ψ_w are engenfunctions of the air and water respectively which can be expressed as

$$\psi_a(\beta_n, z) = A_{a,n} \sin\left(\frac{z}{\sqrt{\nu_a}}\beta_n\right) + B_{a,n} \cos\left(\frac{z}{\sqrt{\nu_a}}\beta_n\right), \tag{B.11}$$

$$\psi_w(\beta_n, z) = A_{w,n} \sin\left(\frac{z}{\sqrt{\nu_w}}\beta_n\right) + B_{w,n} \cos\left(\frac{z}{\sqrt{\nu_w}}\beta_n\right), \tag{B.12}$$

and the eigenvalue β_n is given by

$$\frac{1 - \sqrt{\frac{\rho_w \mu_w}{\rho_a \mu_a}}}{1 + \sqrt{\frac{\rho_w \mu_w}{\rho_a \mu_a}}} \cos\left[\left(\frac{h}{\sqrt{\nu_w}} - \frac{h}{\sqrt{\nu_a}}\right)\beta_n\right] + \cos\left[\left(\frac{h}{\sqrt{\nu_w}} + \frac{h}{\sqrt{\nu_a}}\right)\beta_n\right] = 0, \tag{B.13}$$

where $A_{a,n}$, $B_{a,n}$, $A_{w,n}$ and $B_{w,n}$ are given by

$$A_{a,n} = -\frac{\cos\left(\frac{\beta_n}{\sqrt{\nu_w}}h\right)\cos\left(\frac{\beta_n}{\sqrt{\nu_a}}2h\right)}{\sin\left(\frac{\beta_n}{\sqrt{\nu_a}}h\right)}, \tag{B.14}$$

$$B_{a,n} = \frac{\cos\left(\frac{\beta_n}{\sqrt{\nu_w}}h\right)\sin\left(\frac{\beta_n}{\sqrt{\nu_a}}2h\right)}{\sin\left(\frac{\beta_n}{\sqrt{\nu_a}}h\right)}, \tag{B.14}$$

$$A_{w,n} = 0, \tag{B.15}$$

$$B_{w,n} = 1. \tag{B.16}$$

For detail deviation, readers are referred to Choy & Reible (2000).

II. Generating turbulence by Buoyancy force

The second step to initiate the simulation flow field is the generation of turbulence. We spin up the turbulence by adding small random perturbations in the air and water temperature fields to the buoyancy force in the *w* momentum equation. The governing equations used to express these flow fields (air and water) are

$$\frac{\partial u_\ell}{\partial x}+\frac{\partial v_\ell}{\partial y}+\frac{\partial w_\ell}{\partial z}=0, \tag{B.17}$$

$$\frac{\partial u_\ell}{\partial t}+\frac{\partial u_\ell^2}{\partial x}+\frac{\partial u_\ell v_\ell}{\partial y}+\frac{\partial u_\ell w_\ell}{\partial z}=-\frac{1}{\rho_\ell}\frac{\partial p_\ell}{\partial x}+\nu_\ell\left(\frac{\partial^2 u_\ell}{\partial x^2}+\frac{\partial^2 u_\ell}{\partial y^2}+\frac{\partial^2 u_\ell}{\partial z^2}\right), \tag{B.18}$$

$$\frac{\partial v_\ell}{\partial t}+\frac{\partial u_\ell v_\ell}{\partial x}+\frac{\partial v_\ell^2}{\partial y}+\frac{\partial v_\ell w_\ell}{\partial z}=-\frac{1}{\rho_\ell}\frac{\partial p_\ell}{\partial y}+\nu_\ell\left(\frac{\partial^2 v_\ell}{\partial x^2}+\frac{\partial^2 v_\ell}{\partial y^2}+\frac{\partial^2 v_\ell}{\partial z^2}\right), \tag{B.19}$$

$$\frac{\partial w_\ell}{\partial t}+\frac{\partial u_\ell w_\ell}{\partial x}+\frac{\partial v_\ell w_\ell}{\partial y}+\frac{\partial w_\ell^2}{\partial z}=-\frac{1}{\rho_\ell}\frac{\partial p_\ell}{\partial z}+\nu_\ell\left(\frac{\partial^2 w_\ell}{\partial x^2}+\frac{\partial^2 w_\ell}{\partial y^2}+\frac{\partial^2 w_\ell}{\partial z^2}\right)+g\alpha_\ell\left(\theta_\ell-\theta_\ell^\circ\right), \tag{B.20}$$

$$\frac{\partial \theta_\ell}{\partial t}+\frac{\partial u_\ell \theta_\ell}{\partial x}+\frac{\partial v_\ell \theta_\ell}{\partial y}+\frac{\partial w_\ell \theta_\ell}{\partial z}=\mathrm{K}_\ell\left(\frac{\partial^2 \theta_\ell}{\partial x^2}+\frac{\partial^2 \theta_\ell}{\partial y^2}+\frac{\partial^2 \theta_\ell}{\partial z^2}\right), \tag{B.21}$$

where α_ℓ is coefficient of thermal expansion, K_ℓ is thermal diffusivity, and $\theta_\ell^\circ=1/\alpha_\ell$ is reference temperature. Again the subscript ℓ denotes variables in air ($\ell=a$) or water ($\ell=w$).

Boundary conditions for temperature fields are described as follows. For four sidewalls of computation domain, periodic boundary conditions are assumed on them. For upper and lower boundaries, constant temperature condition is applied as

$$\theta_a(x,y,z=h,t)=\theta_1, \tag{B.22}$$

$$\theta_w(x,y,z=-h,t)=\theta_2, \tag{B.23}$$

where $\theta_1>\theta_2$. For the boundary at the interface of air and water domain, the linearized conditions for this boundary are continuity of temperature and heat flux. The expressions of these interfacial boundary conditions are

$$\theta_a=\theta_w, \tag{B.24}$$

$$\frac{\partial \theta_a}{\partial z} = \frac{\hbar_w}{\hbar_a} \frac{\partial \theta_w}{\partial z}, \tag{B.23}$$

where $\hbar_a = \mathrm{K}_a \rho_a C_p^a$ and $\hbar_w = \mathrm{K}_w \rho_w C_p^w$ are thermal conductivity of the air and water, and C_p^a and C_p^w are heat capacity of the air and water.

Boundary conditions for velocity fields are described as in section II.3.

Appendix C

Decomposition of the flow field in the Water

Wave motions are generated at the air-water interface and their effect is larger in the water than in the air. And because the flow field in the water is nearly irrotational, it is easier to decompose into ensemble, wave-correlated and wave-uncorrelated turbulent components as

$$f(x,y,z,t) = \langle f \rangle(z) + f^{w}(x,y,z,t) + f^{t}(x,y,z,t). \tag{C.1}$$

The ensemble component $\langle f \rangle(z)$ is defined as averages over horizontal space and time; the wave-correlated component $f^{w}(x,y,z,t)$ is defined as those directly affected by the surface wave motion, which will be described below, and the remainder is turbulent component. Decomposing the flow field in the air is much harder so we will leave it for future study.

The wave-correlated motions $f^{w}(x,y,z,t)$ are the flow fields induced by and move with the surface wave $\eta^{w}(x,y,t)$. The wave component of the surface wave $\eta^{w}(x,y,t)$ is a filtered field of the total wave height $\eta(x,y,t)$. We assume that high frequency potion of the wave height is associated with (or generated by) the turbulence. The cutoff frequency is chosen to be where the energy spectrum $\Phi(\eta)$ has a significant drop. The wave component $\eta^{w}(x,y,t)$ is used to determine the wave-induced velocity and pressure fields in the water. Because the wave-induced motion in the water is nearly irrotational, we can establish a linear relation between the surface wave and the wave-induced motions as follows. The first step uses the analytical solution of sinusoidal waves on deep water. For an irrotational motion, a velocity potential $\phi^{w}(x,y,z,t)$ exists and the wave-induced velocity and pressure satisfy

$$\left(u_w^w, v_w^w, w_w^w\right) = \left(\frac{\partial \phi^w}{\partial x}, \frac{\partial \phi^w}{\partial y}, \frac{\partial \phi^w}{\partial z}\right) \tag{C.2}$$

and

$$p_w^w(x,y,z,t) = -\frac{\partial \phi^w}{\partial t} \tag{C.3}$$

where the suberscript w represents variables in the water domain and the supscript w

represents wave-induced motions. The associated solution of potential function $\phi^w(x,y,z,t)$ is related to the wave height $\eta^w(x,y,t)$ as

$$\phi^w(x,y,z,t) = \Phi(z)e^{i\alpha_t}\eta^w(x,y,t) \tag{C.4}$$

where $\Phi(z)$ is a vertical distribution function and α_t represents a 90° phase lag in time between $\phi^w(x,y,z,t)$ and $\eta^w(x,y,t)$. From $\phi^w(x,y,z,t)$, we can then compute the wave-induced velocity and pressure from equations (C.2) and (C.3). Note that there is also another 90° phase lag between (u_w^w, v_w^w) and $\phi^w(x,y,z,t)$ in (x,y), respectively, according to (C.2). For more detail derivation and description, readers are referred to Lighthill(1978).

In the second step, we obtain the vertical distribution function $\Phi(z)$ by looking at the correlations between the simulated flow fields in the water to the surface wave height component, as follows:

$$\Phi_u(z) = \frac{Co(u_w, \eta_{xt}^w)}{Spec(\eta_{xt}^w, \eta_{xt}^w)}, \tag{C.5}$$

$$\Phi_v(z) = \frac{Co(v_w, \eta_{yt}^w)}{Spec(\eta_{yt}^w, \eta_{yt}^w)}, \tag{C.6}$$

$$\Phi_w(z) = \frac{Co(w_w, \eta_t^w)}{Spec(\eta_t^w, \eta_t^w)}, \tag{C.7}$$

and

$$\Phi_p(z) = \frac{Co(p_w, \eta^w)}{Spec(\eta^w, \eta^w)}, \tag{C.8}$$

where the symbols *Co* and *Spec* represent cross-spectrum and power-spectrum of variables in bracket. For the u component we correlate it with x and t derivatives of $\eta^w(x,y,t)$ (denoted as η_{xt}^w), which yields a 90° phase lag in both x and time t, consistent with equations (C.2) and (C.4). Similarly, the $v_w^w(x,y,z,t)$ field has a 90° phase lag in y with $\phi^w(x,y,z,t)$, and then a 90° phase lag in t with $\eta^w(x,y,t)$. For the w-component, we consider just the 90° time lag between w and $\eta^w(x,y,t)$. The pressure field has no phase lag with $\eta^w(x,y,t)$, according to (C.3) and (C.4). The correlation analysis

shown in equations (C.5)-(C.8) yields a height dependence of the correlation between the flow field and the surface wave height; the closer to the surface, the larger the correlation.

Figures 22-25 show the application of this method on surface wave height, streamwise velocity, spanwise velocity and vertical velocity at the interface. Different cutoff frequency and wavenumber are chosen to be where the energy spectrum $\Phi(\eta)$ has a significant drop and the energy spectrum $\Phi(\eta)$ contains most of the wave energy. No significant change on u^t and v^t components, but the distribution of η^t and w^t is more irregular.

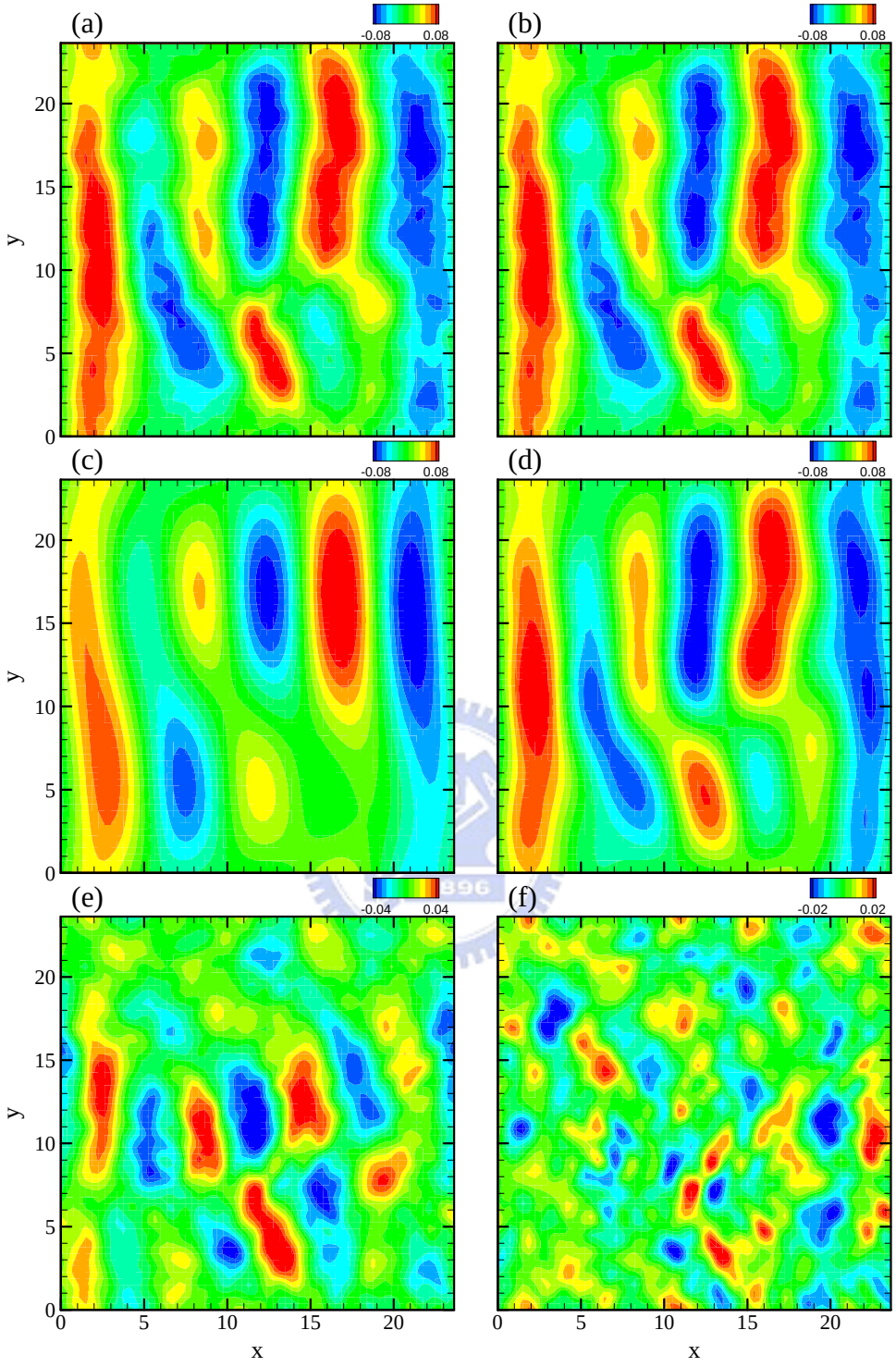

Figure 22. The decomposition of surface wave height near time t~65 s. With the application of decomposition method in Appendix C, the total surface wave height (*a*, *b*) can split into wave-correlated components (*c*, *d*) and wave-uncorrelated components (*e*, *f*). The difference between left and right columns is the cutoff frequency (or wavenumber). The cutoff frequency (wavenumber) of left column is smaller (larger) than right column.

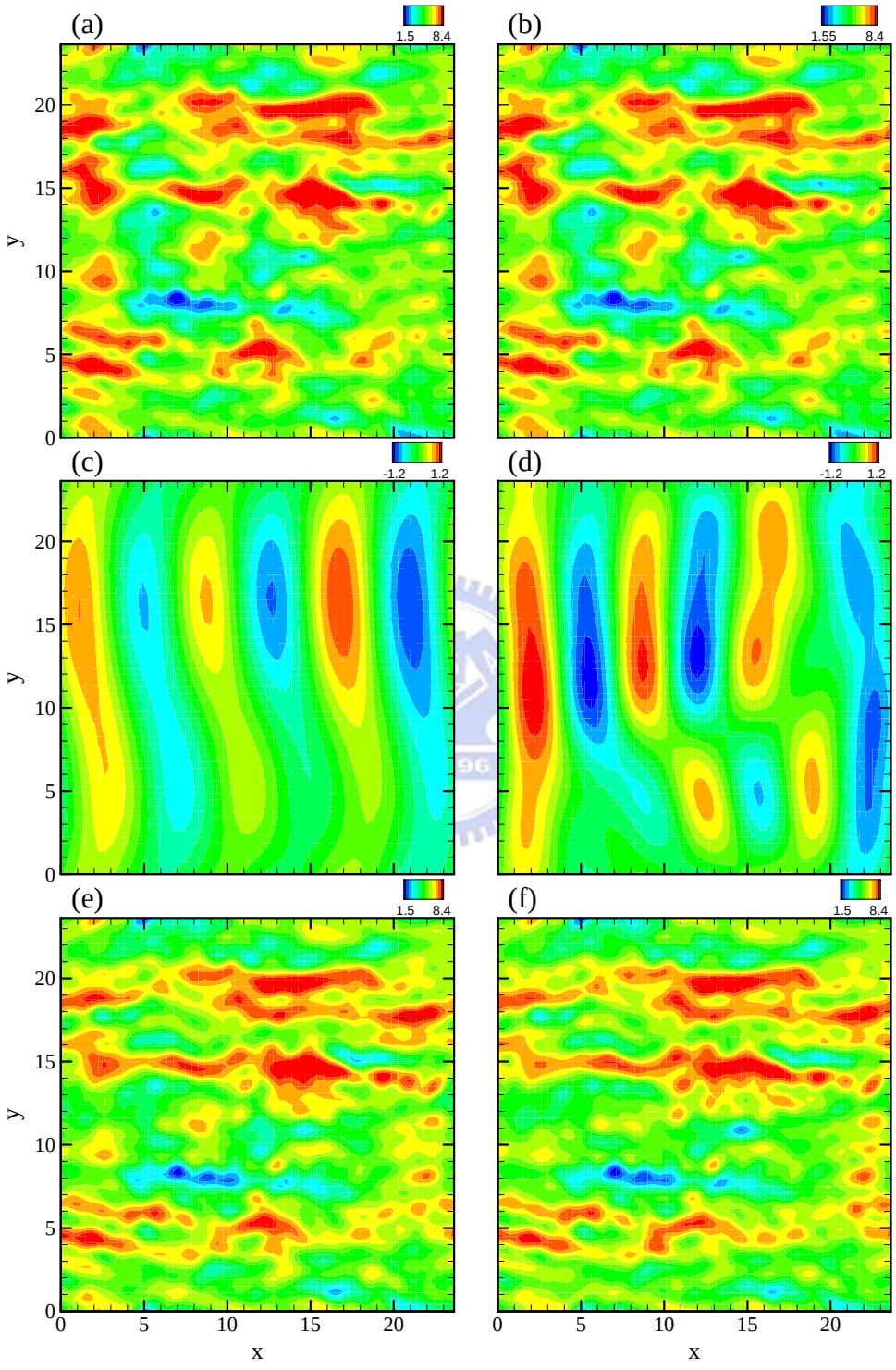

Figure 23. As figure 22 but for the decomposition of streamwise velocity at the interface.

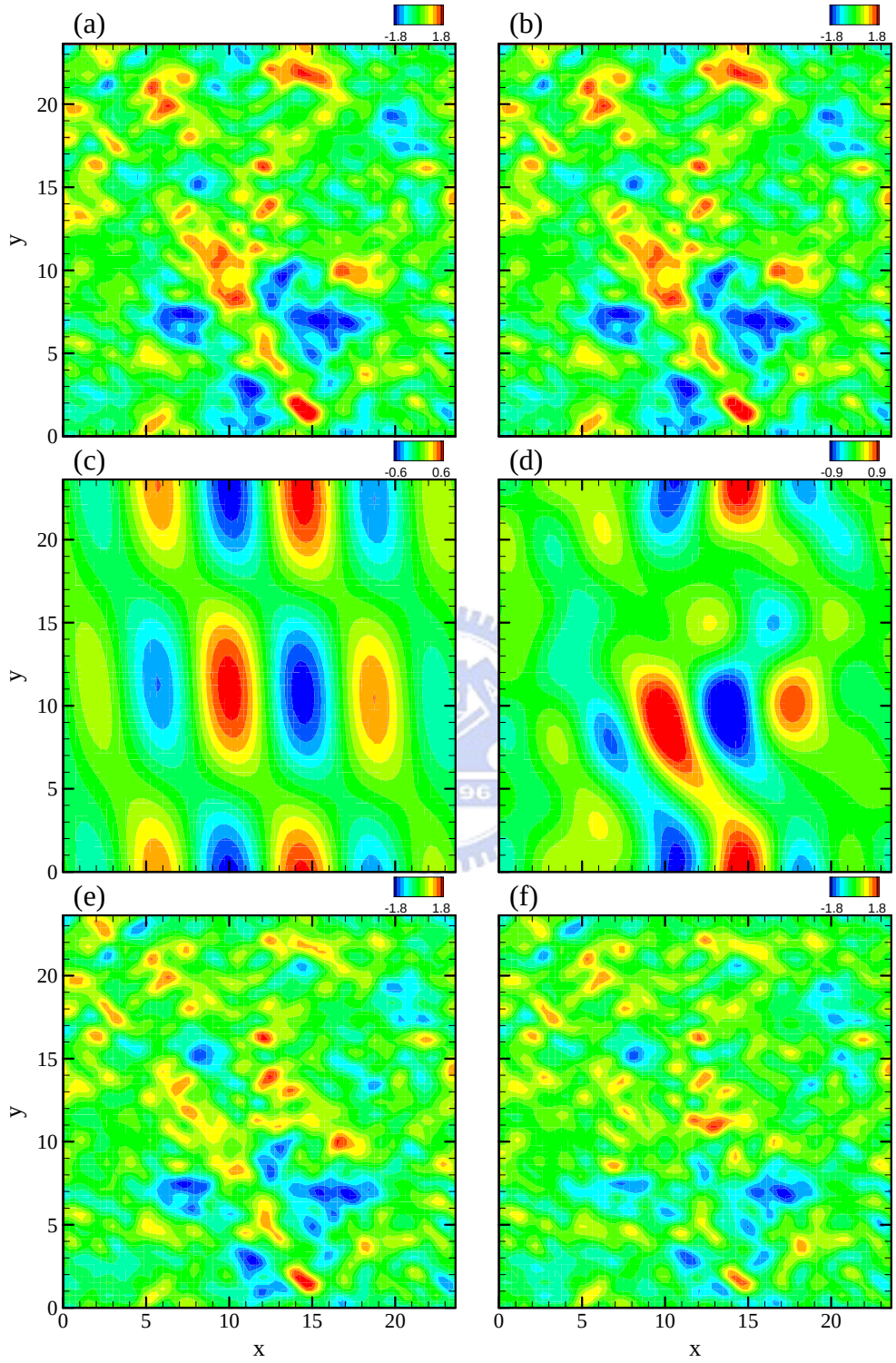

Figure 24. As figure 22 but for the decomposition of spanwise velocity at the interface.

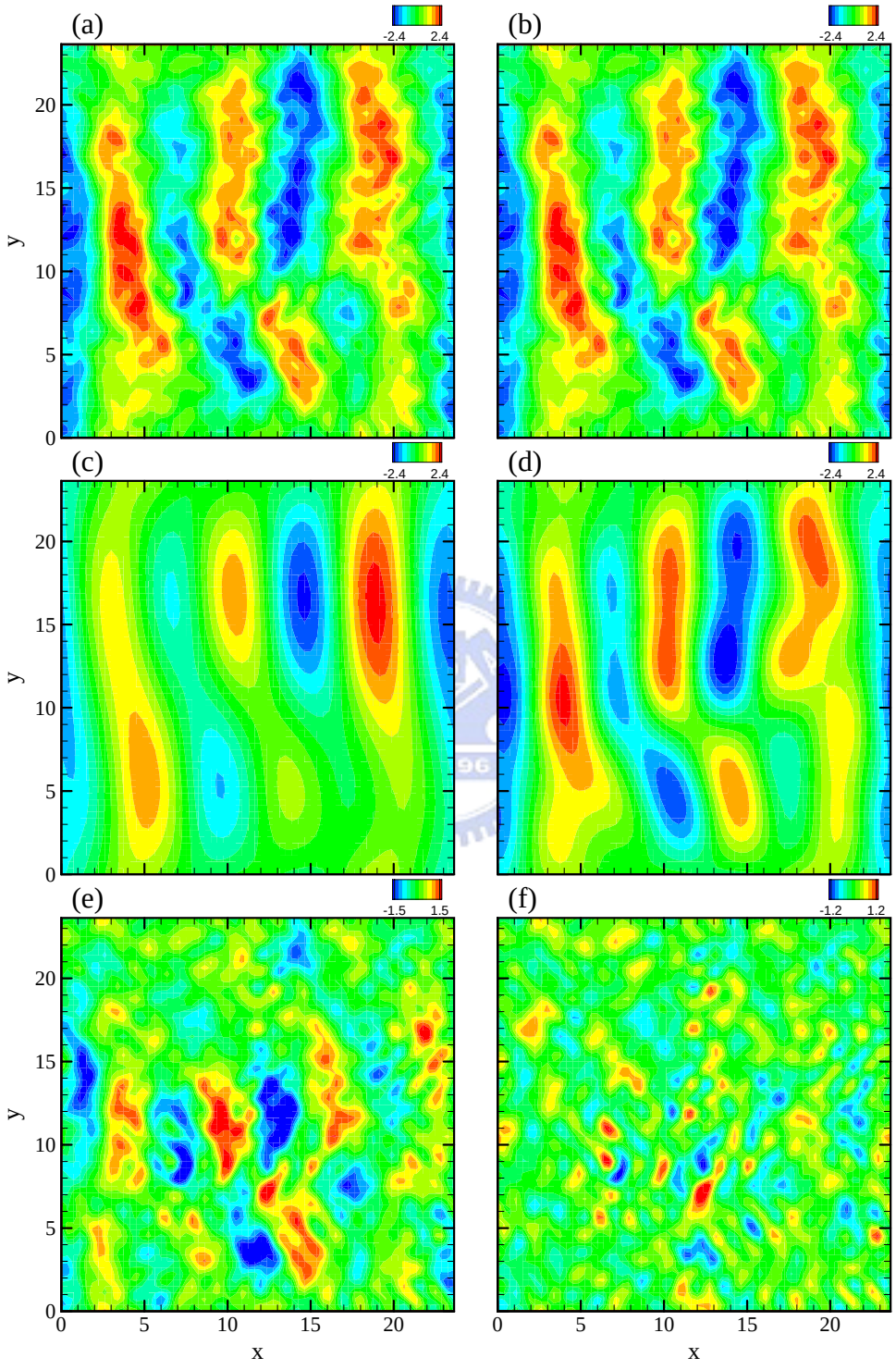

Figure 25. As figure 22 but for the decomposition of vertical velocity at the interface.

Appendix D

Some records for four simulation runs

Some analytic results for four simulation runs are recorded in this section.

Figure 26 shows the time evolution of mean wind stress of four simulation runs. As described in previous section, the nearly constant mean wind stress represents that the air-water coupled flow reaches a statistically quasi-steady state in respond to the wind forcing. Furthermore, the distribution of mean vertical turbulent flux, viscous flux and their sum of the wind field (figure 27) has similar behaviour of a Couette flow under a steady condition. Therefore, these four simulation runs reach the state of fully-developed, wind-driven turbulent flow.

Figures 28-30 show that the simulations with no initial turbulence in the water, no surface tension at the interface and the height of the air domain h = 8 cm also observe the phenomena of waves and streaks. Also, the dominate waves for these four simulation runs are different (tables 1-4).

Compare wavenumber spectra of pressure fluctuations of the air (figure 31) with wavenumber spectra of surface wave height (figure 21), the result shows that the peaks of their energy distribution do not coincide with each other at early stage but are at the same wave components at late stage. This interprets that pressure field has different behaviours at early and late stage. One is turbulent-induced components dominated at early stage that do not correlate with surface waves, and the other is wave-induced components dominated at late stage that correlate with surface waves.

Time evolution of some flow quantities at the interface for other three runs (figure 32-34) also has similar results as control run. For surface wave height $\langle \eta^2 \rangle^{1/2}$, it grows slowly before $t \sim 40\,\mathrm{s}$ and fast after $t \sim 40\,\mathrm{s}$. For other flow quantities, they are nearly constant before $t \sim 40\,\mathrm{s}$ and then increase sharply with time except for the mean surface current U_s of the run with no initial turbulence in the water. It increases with time before

t~60 s and decreases with time after *t*~60s.

Figures 35 and 36 show that time evolution of wave amplitude and form stress of the simulations with no initial turbulence in the water, no surface tension at the interface and the height of the air domain h = 8 cm have different behaviour as described in section VI at early and late stages. However, for wave components those grow much slower than the fastest growing wave in these two stages will not have the same behaviour. In linear growth stage, for example, wave component $(k_x, k_y) = (0.78,0.)\ \mathrm{cm}^{-1}$ of the simulation with larger air height, does not have linear wave growth trend. And in exponential growth stage, the form stress of wave components $(k_x, k_y) = (0.52,0.26)$ and $(0.78,0.26)\mathrm{cm}^{-1}$ of the simulation with no initial turbulence in the water and larger air height respectively do not have exponential growth trend.

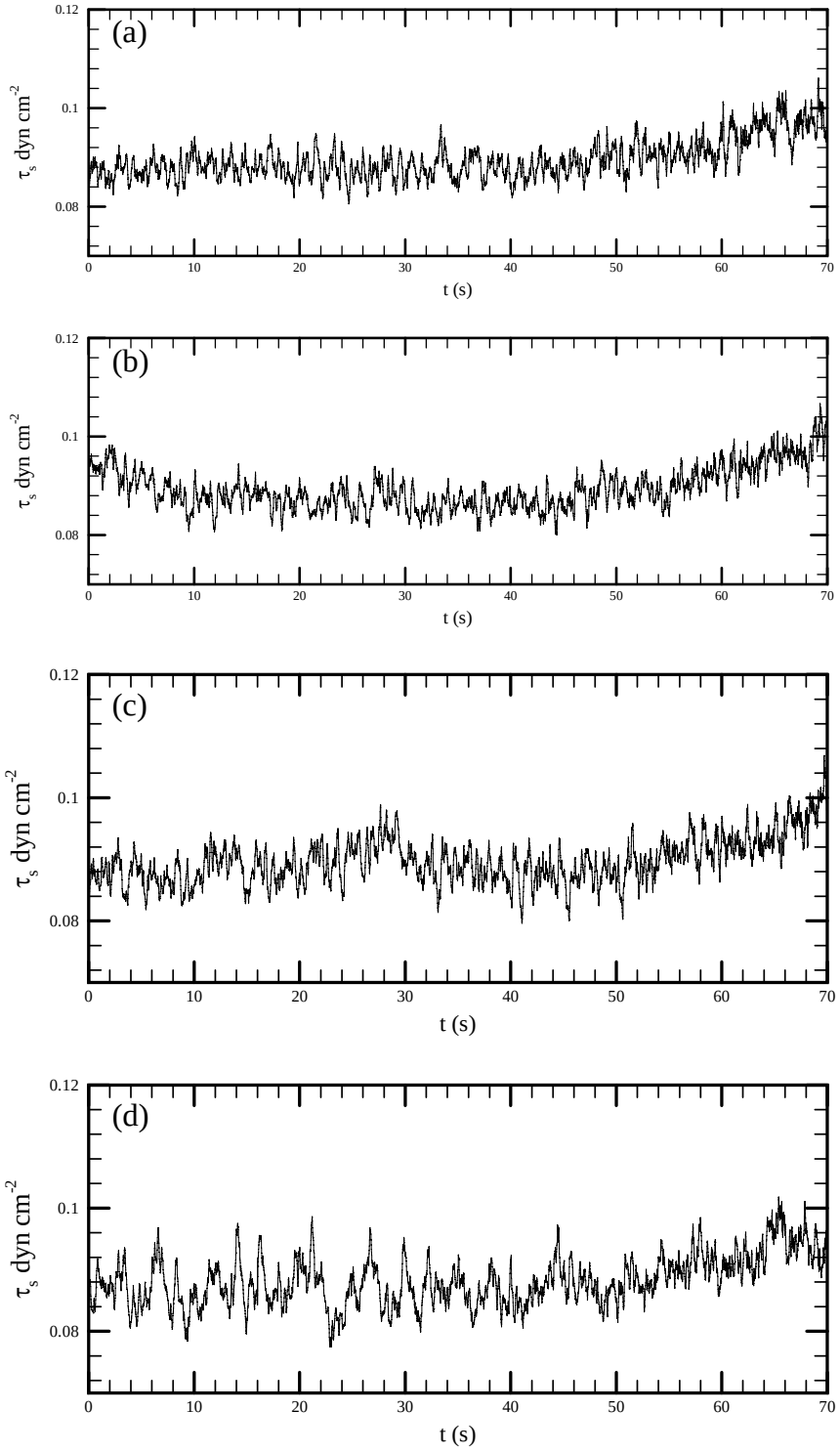

Figure 26. As figure 3 but for (*a*) the control run with the height of the air domain h = 4 cm, (*b*) the run with no initial turbulence in the water, (*c*) the run with no surface tension and (*d*) the run with the height of the air domain h = 8 cm.

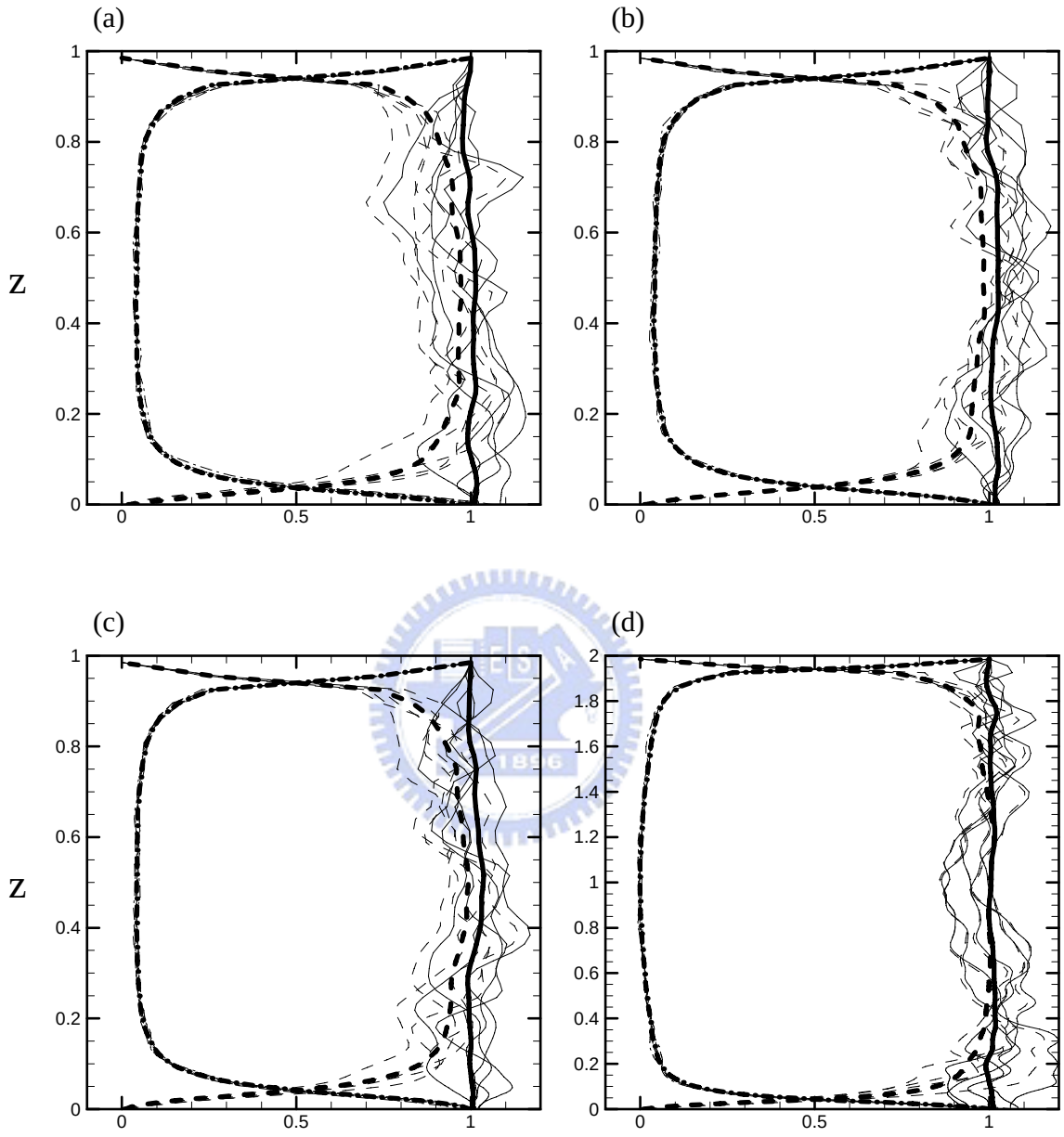

Figure 27. As figure 4 but for (*a*) the control run with the height of the air domain h = 4 cm, (*b*) the run with no initial turbulence in the water, (*c*) the run with no surface tension and (*d*) the run with the height of the air domain h = 8 cm.

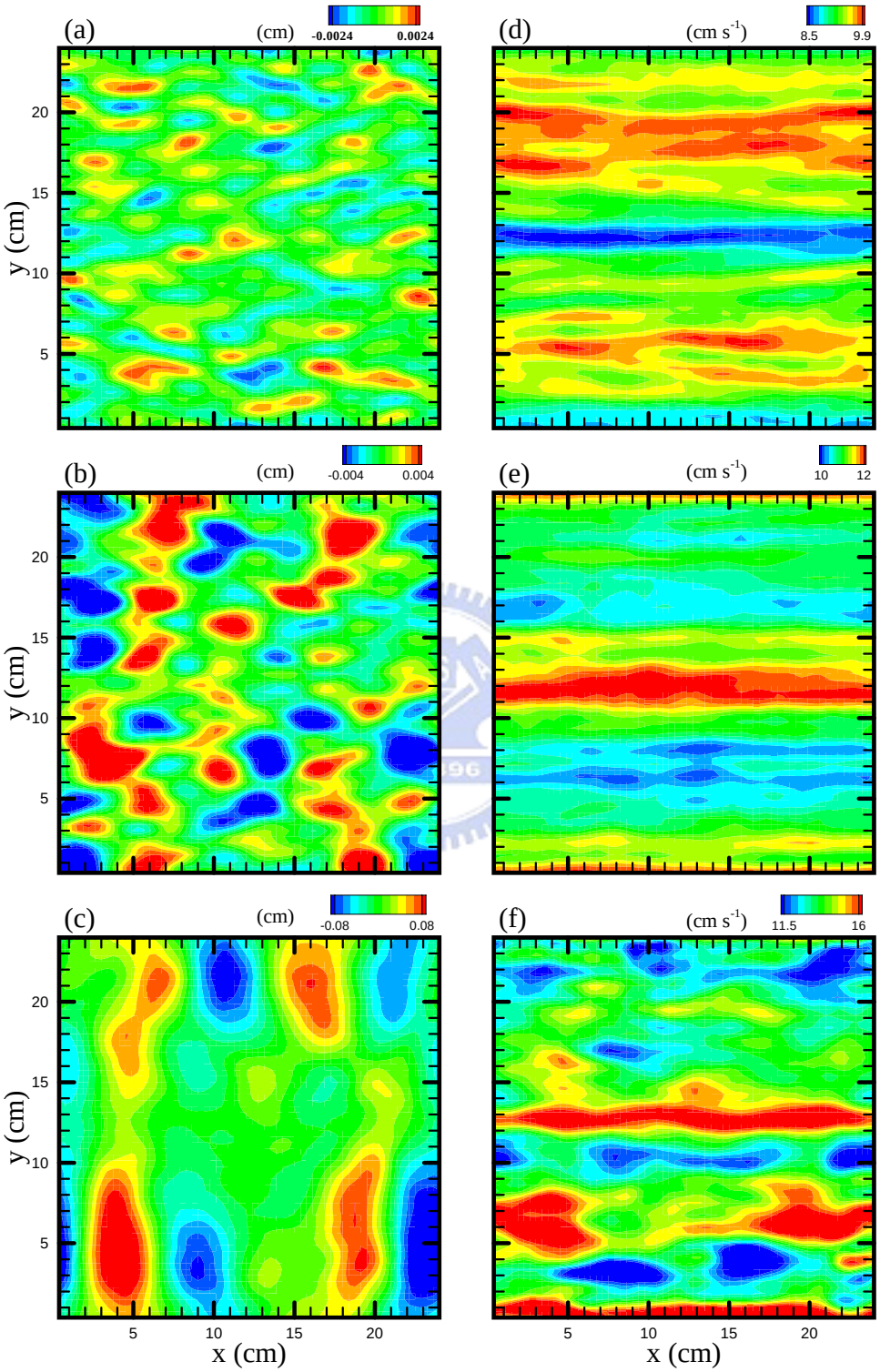

Figure 28. As figure 5 but for the run with no initial turbulence in the water.

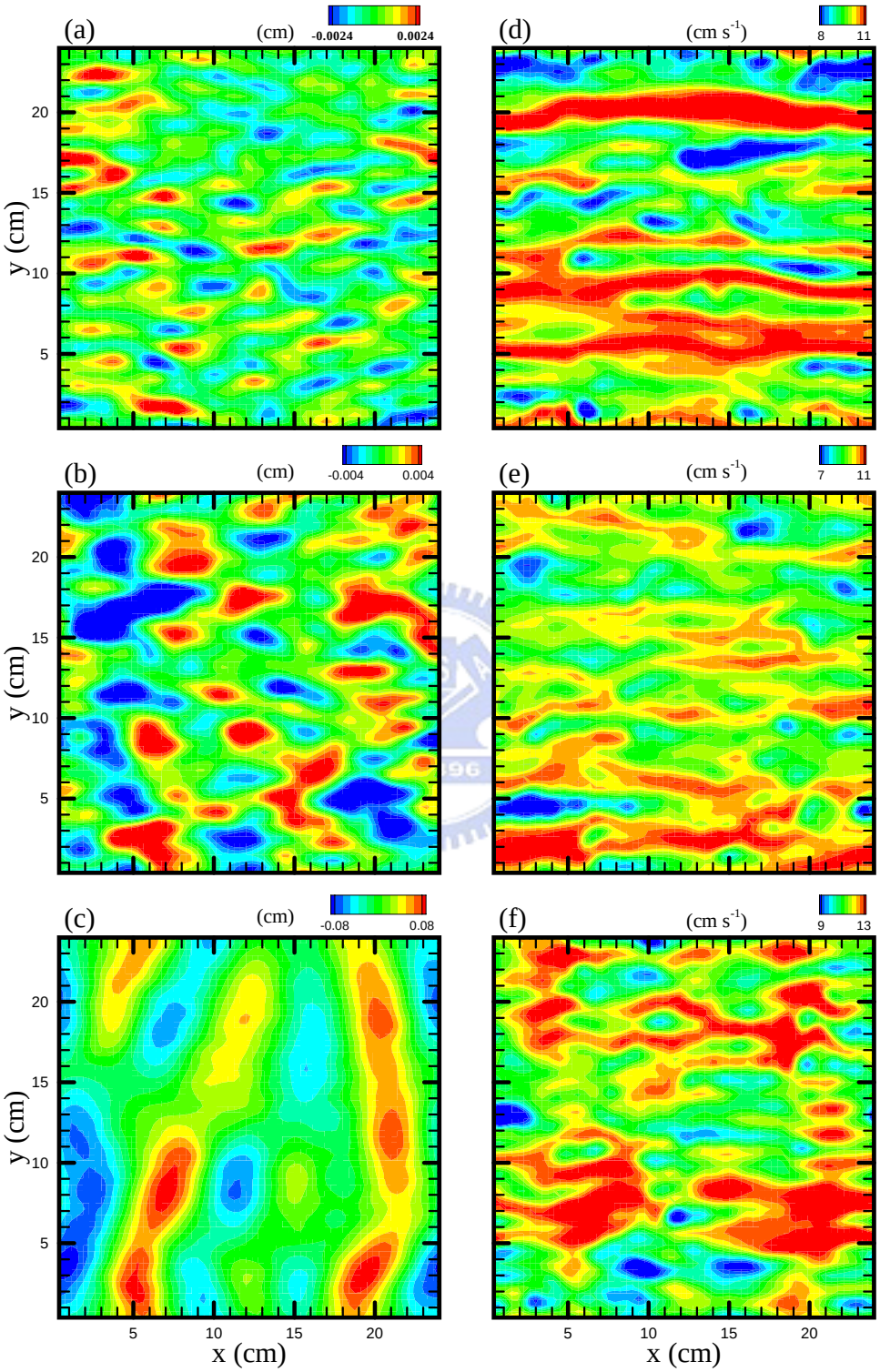

Figure 29. As figure 5 but for the simulation without surface tension at the interface.

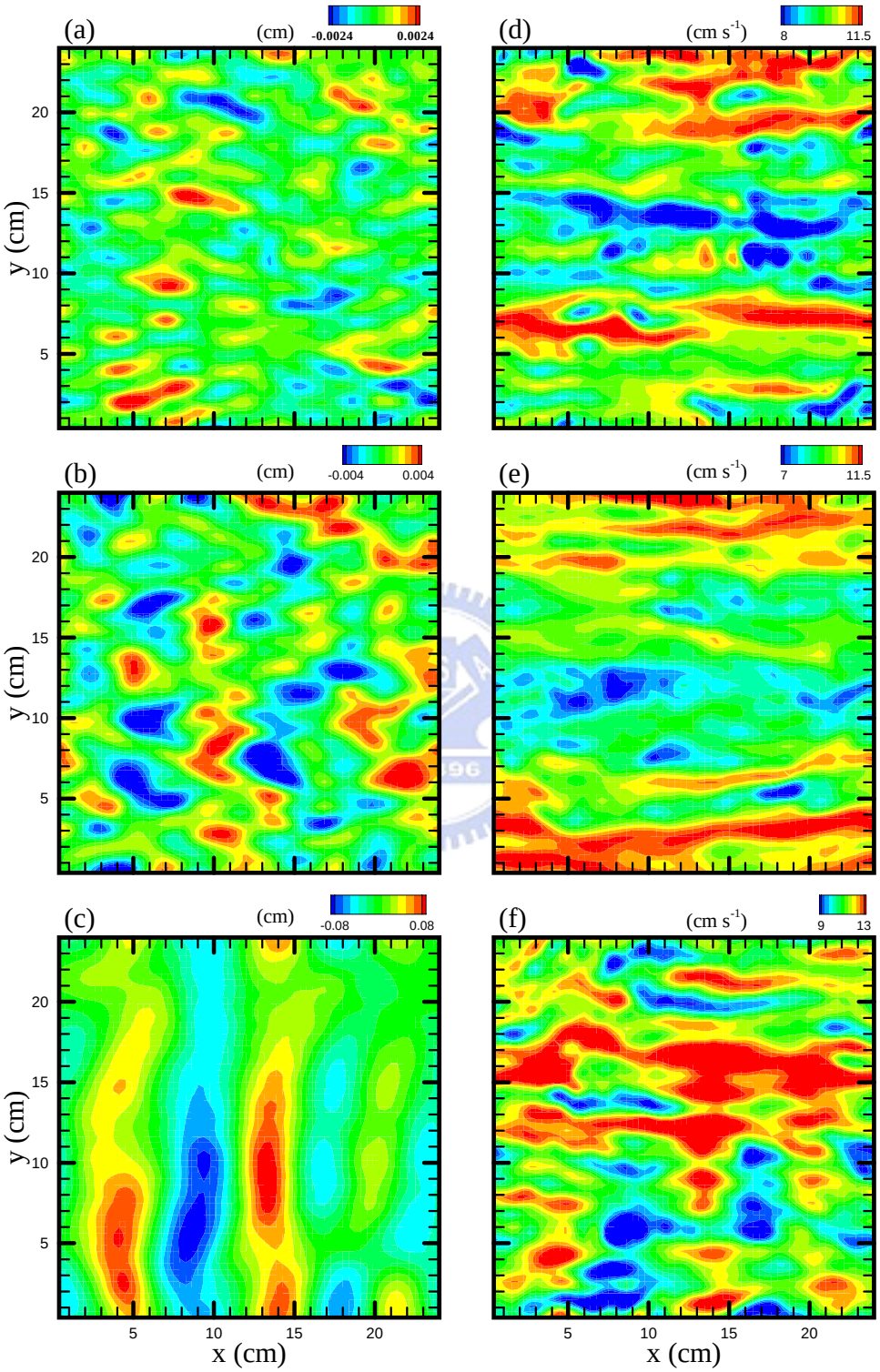

Figure 30. As figure 5 but for the simulation doubling the height of the computational domain of the air.

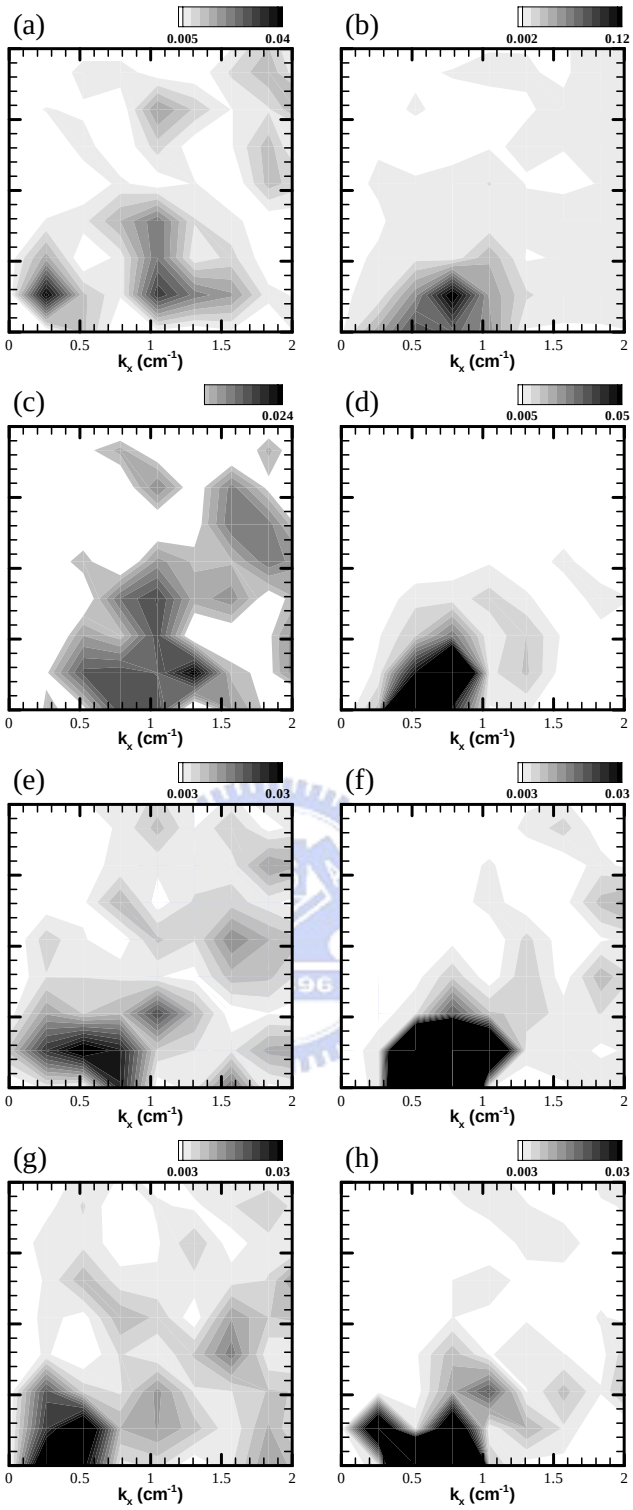

Figure 31. Wavenumber spectra of surface pressure fluctuations of the air (normalized by its total energy) at time $t = 16\,\mathrm{s}$ (left panels) and $t = 64\,\mathrm{s}$ (right panels) for the control case shown in (*a*, *b*), the simulation without generating turbulence in the water at the beginning of the simulation shown in (*c*, *d*), the simulation without surface tension at the interface in (*e*, *f*), and the simulation doubling the height of the computational domain of the air in (*g*, *h*).

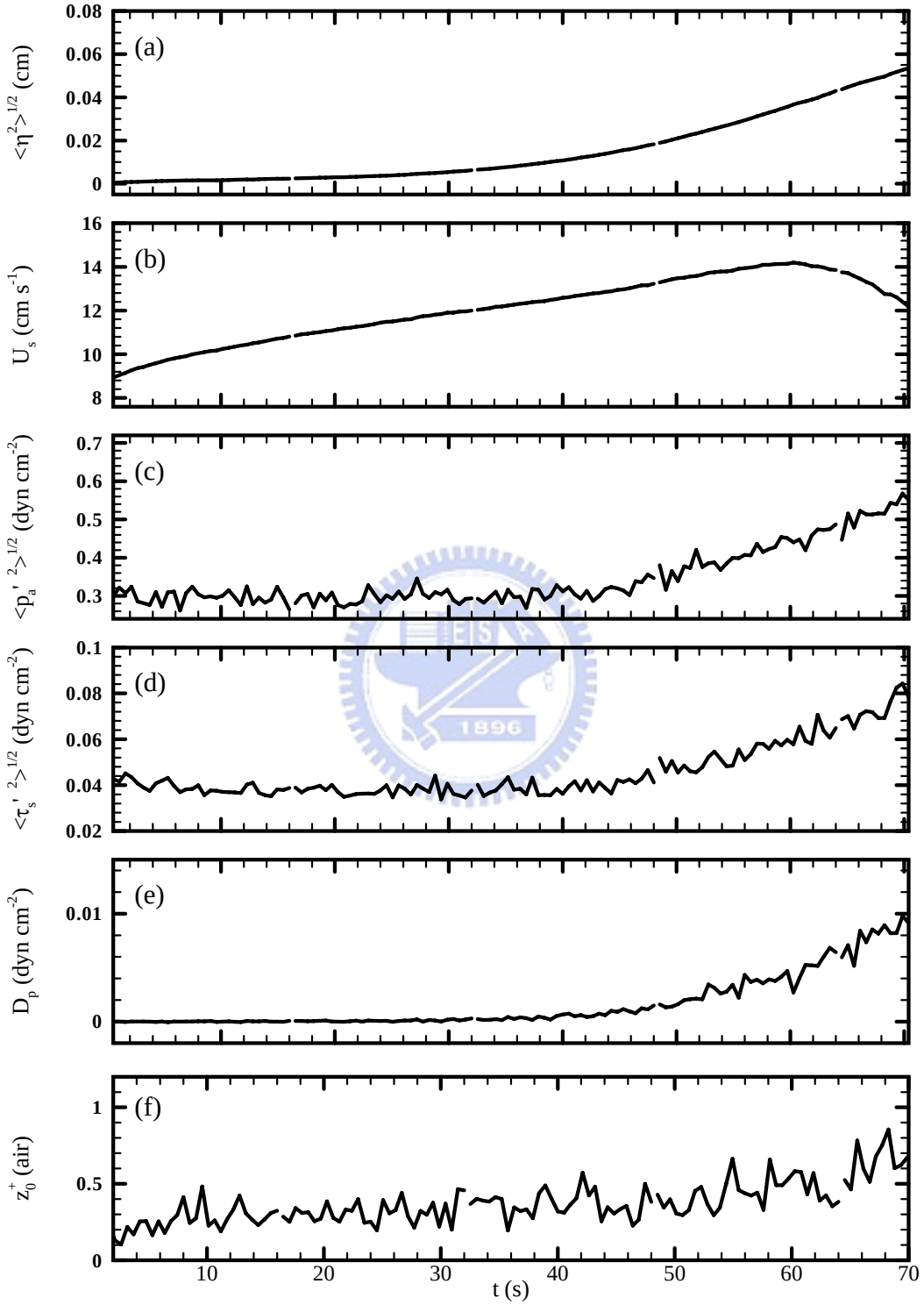

Figure 32. As figure 16 but for the run with no initial turbulence in the water.

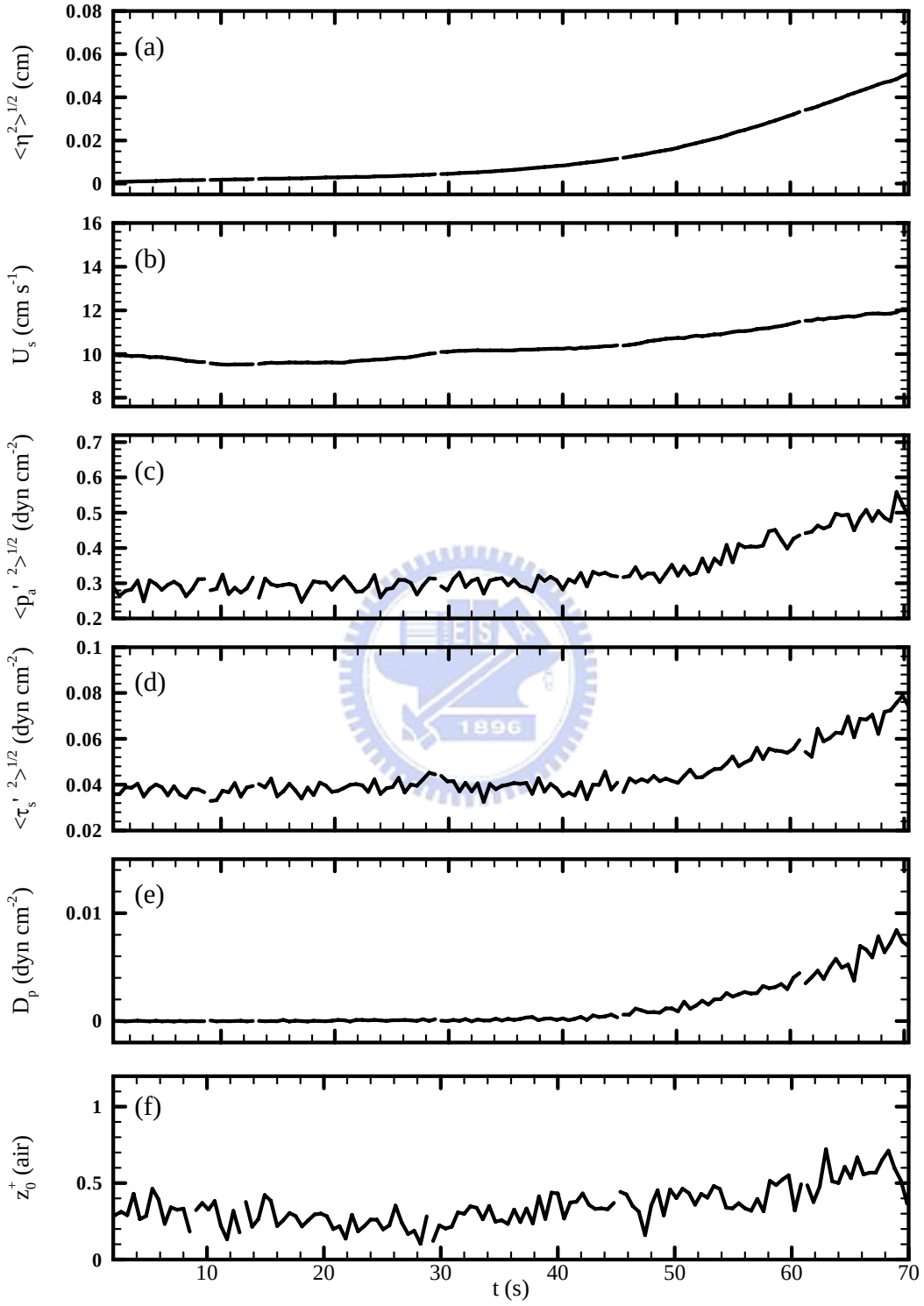

Figure 33. As figure 16 but for the simulation without surface tension at the interface.

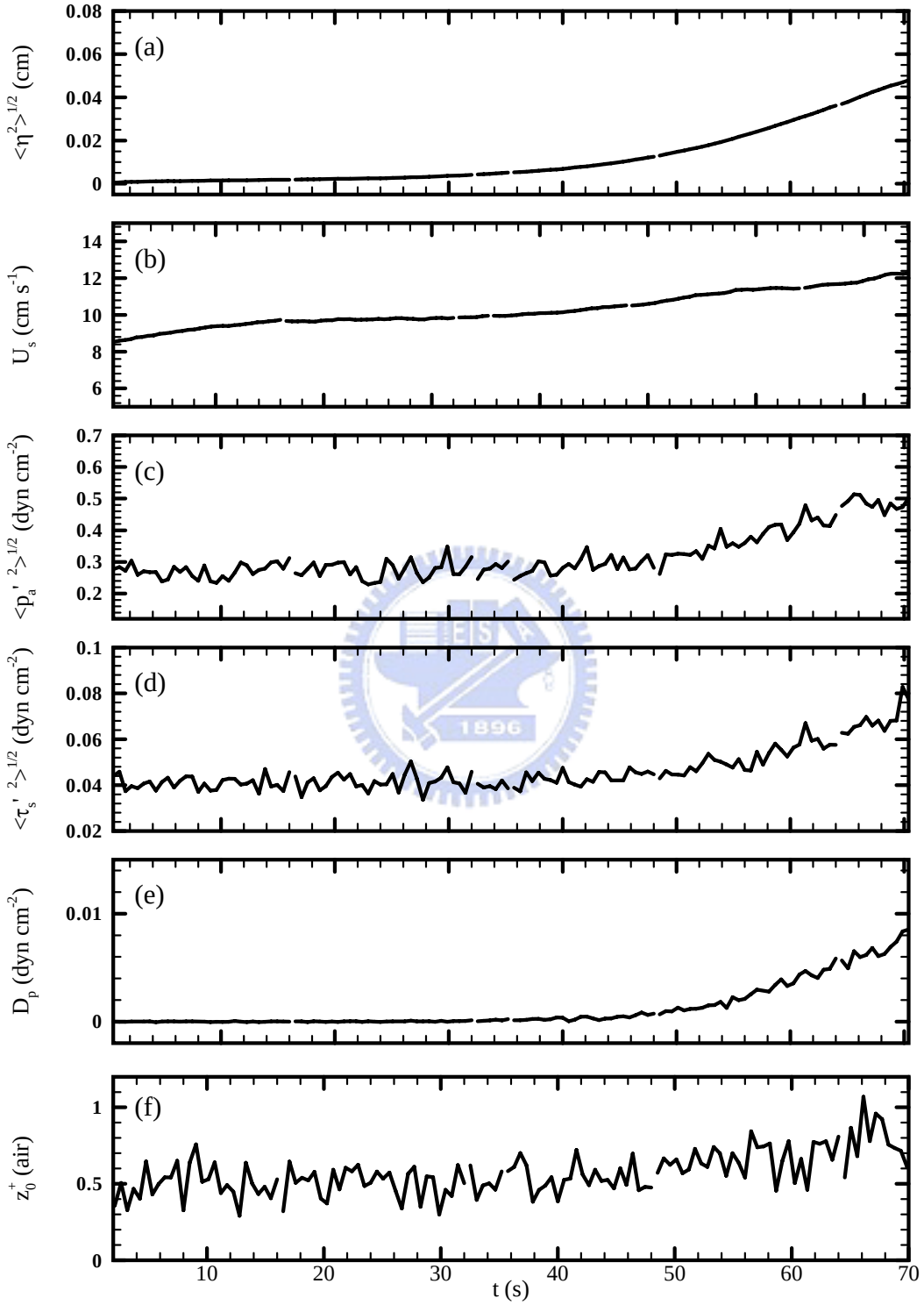

Figure 34. As figure 16 but for the simulation doubling the height of the computational domain of the air.

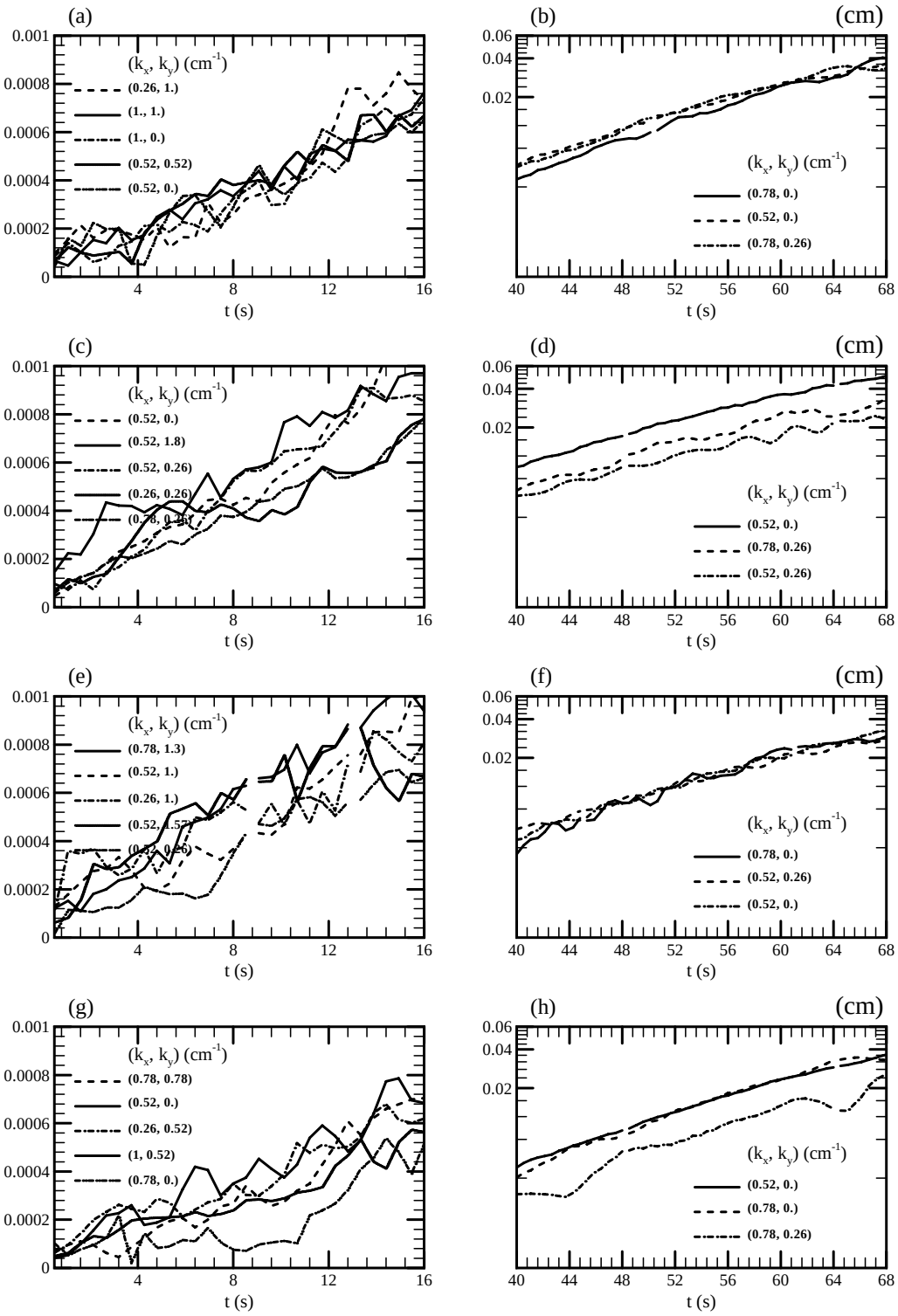

Figure 35. As figure 17 but for the control case shown in (*a*, *b*), the simulation without generating turbulence in the water at the beginning of the simulation shown in (*c*, *d*), the simulation without surface tension at the interface in (*e*, *f*), and the simulation doubling the height of the computational domain of the air in (*g*, *h*).

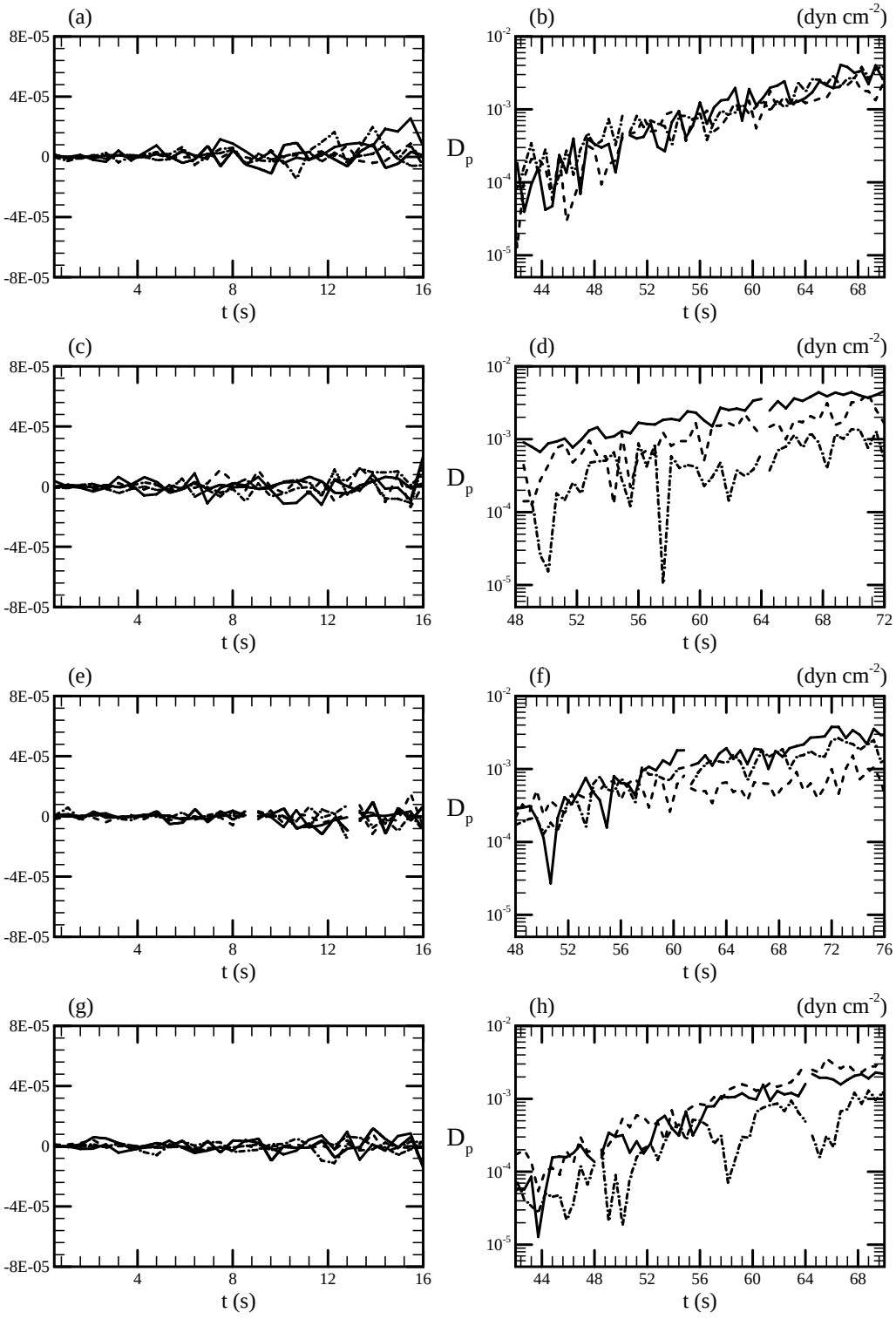

Figure 36. As figure 18 but for the control case shown in (*a*, *b*), the simulation without generating turbulence in the water at the beginning of the simulation shown in (*c*, *d*), the simulation without surface tension at the interface in (*e*, *f*), and the simulation doubling the height of the computational domain of the air in (*g*, *h*).

	Wave number $\kappa = (k_x, k_y)$ (cm^{-1})	$\Phi(\eta)/<\eta^2>^{1/2}$
t ~ 15 s	(0.52, 0.)	11 %
	(0.52, 1.83)	9.7 %
	(1.52, 0.26)	8.5 %
	(0.26, 0.26)	7.8 %
	(0.78, 0.26)	7.3 %
t ~ 68 s	(0.52, 0.)	50 %
	(0.78, 0.26)	20 %
	(0.52, 0.26)	9.8 %

Table 2 Dominate waves and the percentage of each wave energy at early (t~15s) and late (t~68 s) stages for the simulation without generating turbulence in the water at the beginning of the simulation.

	Wave number $\kappa = (k_x, k_y)$ (cm^{-1})	$\Phi(\eta)/<\eta^2>^{1/2}$
t ~ 15 s	(0.78, 1.3)	9 %
	(0.52, 1.)	8.6 %
	(0.26, 1.)	5.3 %
	(0.52, 1.57)	4.7 %
	(0.52, 0.26)	4.1 %
t ~ 68 s	(0.78, 0.)	27 %
	(0.52, 0.26)	22 %
	(0.52, 0.)	19 %

Table 3 Dominate waves and the percentage of each wave energy at early (t~15s) and late (t~68 s) stages for the simulation without surface tension effect.

	Wave number $\kappa = (k_x, k_y)$ (cm^{-1})	$\Phi(\eta)/<\eta^2>^{1/2}$
t ~ 15 s	(0.78, 0.78)	8.3 %
	(0.52, 0.)	6.2 %
	(0.26, 0.52)	5.1 %
	(1., 0.52)	4.9 %
	(0.78, 0.)	4.6 %
t ~ 68 s	(0.52, 0.)	31 %
	(0.78, 0.)	28 %
	(0.78, 0.26)	13 %

Table 4 Dominate waves and the percentage of each wave energy at early (t~15s) and late (t~68 s) stages for the simulation with larger air domain.

Appendix E

Future Work

Some future work of the present study is introduced as follows.

First, apply message-passing interface (MPI) method to make this code has ability of doing parallel computing. This can solve the problem of the limitation of computer power. For example, we need 6 weeks to finish a run with one processor where 2.4 GHz CPU is used and 2×64^3 gridpoints are calculated. If the MPI method is applied, the reduction rate of the calculating time will decrease according to how many processors are used at the same time.

Second, we need to do some sensitivity tests of larger computation domain and stronger wind forcing. After this code can do parallel computing, it will become practicable to realize the effect of computation domain and wind forcing on wind-wave generation processes.

Third, temperature is also an important factor to influence wave growth. The effect of stable, neutral and unstable stratosphere on wind-wave generation processes will also be an interesting topic.

Last, this coupled model also has its limitation due to the linearized interfacial boundary conditions and the use of direct numerical simulation method. When linearized interfacial boundary conditions are used, this coupled model can not simulate wave breaking effect, wave-wave interaction and large amplitude wave where wave slope greater than 0.01. And when direct numerical simulation is used, it is unable to simulate mesoscale and macroscale motions with present computer power. Therefore, use other simulation scheme or nonlinear interfacial boundary conditions can extend the application of this study to more variety topics.

References

1. AL-ZANAIDI, M. A. & HUI, W. H. 1984 Turbulent airflow over water waves – a numerical study. *J. Fluid Mech.* **148**, 225-246.
2. AYDIN, E. M. & LEUTHEUSSER, H. J. 1991 Plane-Couette flow between smooth and rough walls. *Exps. Fluids* **11**, 302-312.
3. BELCHER, S. E., NEWLEY, T. M. J. & HUNT, J. C. R. 1993 The drag on an undulating surface due to the flow of a turbulent layer. *J. Fluid Mech.* **249**, 557-596.
4. BELCHER, S. E. & HUNT, J. C. R. 1993 Turbulent shear flow over slowly moving waves. *J. Fluid Mech.* **251**, 109-148.
5. CHANDRASEKHAR, S. 1954 The character of the equilibrium of an incompressible heavy viscous fluid of variable density. Quart. J. Mech. 162-178.
6. CHEUNG, T. K. & STREET, R. L. 1988 The turbulent layer in the water at an air-water interface. *J. Fluid Mech.* **194**, 133-151.
7. CHOY & REIBLE 2000 *Diffusion model of environmental transport*, Lewis Publishers (Boca, Raton, London, New York)
8. DAVIS, R. E. 1970 On the turbulent flow over a wavy boundary. *J. Fluid Mech.* **42**, 721-731.
9. DE ANGELIS, V., LOMBARDI, P. & BANERJEE, S. 1997 Direct numerical simulation of turbulent flow over a wavy wall. *Phys. Fluids* **9**, 2429-2442.
10. DE ANGELIS, V. 1998 Numerical investigation and modeling of mass transfer processes at sheared gas-liquid interface. PhD Thesis, UCSB.
11. ELLIOTT, J. A. 1972a Microscale pressure fluctuations measured within the atmospheric boundary layer. *J. Fluid Mech*. **53**, 351-384.
12. ELLIOTT, J. A. 1972b Microscale pressure fluctuations near waves being generated by the wind. *J. Fluid Mech*. **54,** 427-448.
13. FULGOSI, M., LAKEHAL, D., BANERJEE, S. & DE ANGELIS, V. 2003 Direct

numerical simulation of turbulence in a sheared air-water flow with a deformable interface. *J. Fluid Mech.* **482**, 319-345.

14. GENT, P. R. & TAYLOR, P. A. 1976. A numerical model of the air flow above water waves. *J. Fluid Mech.* **77**, 105-128.
15. HENN, D. S. & SYKES, R. I. 1999 Large-eddy simulation of flow over wavy surface. *J. Fluid Mech.* **383**, 75-112.
16. HOWE, B. M., CHAMBERS, A. J., KLOTZ, S. P., CHEUNG, T. K. & STREET, R. L. 1982 Comparison of profiles and fluxes of heat and momentum above and below an air-water interface. *Trans. ASME C: J. Heat Transfer* **104**, 34-39.
17. JACOBS, S. J. 1987 An asymptotic theory for the turbulent flow over a progressive wave. *J. Fluid Mech.* **174**, 69-80.
18. JEFFREYS, H. 1925 On the formation of water waves by wind. *Proc. R. Soc. Lond.* A **107**, 189-206.
19. KAHMA, K. K. & DONELAN, M. A. 1988 A laboratory study of the minimum wind speed for wind wave generation. *J. Fluid Mech.* **192**, 339-364.
20. KIM, J. MOIN, P. & MOSER, R. 1987 Turbulence statistics in fully developed channel flow at low Reynolds number. *J. Fluid Mech.* **177**, 133-166.
21. LI, P.Y. 1995 A numerical study on energy transfer between turbulent air flow and finite amplitude water waves. PhD Thesis, York University.
22. LIGHTHILL, M. J. 1962 Physical interpretation of the mathematical theory of wave generation by wind. *J. Fluid Mech.* **14**, 385-398.
23. LIGHTHILL, M. J. 1978 *Waves in Fluids*. Cambridge University Press.
24. LOMBARDI, P., DE ANGELIS, V. & BANERJEE S. 1996 Direct numerical simulation of near-interface turbulence in coupled gas-liquid flow. *Phys. Fluids* **8**, 1643-1665.
25. MASSEL, S. R. 1996 *Ocean surface waves: their physics and prediction.* World Scientific Publishing Co.
26. MILES, J. W. 1957 On the generation of surface waves by shear flows. *J. Fluid Mech.* **3**, 185-204.

27. MOIN, P., MAHESH, K. 1998 Direct numerical simulation: A tool in turbulence research. *Annu. Rev. Fluid Mech*. **30**, 539-578.

28. PAPAVASSILIOU, D. V. & HANRATTY, T. J. 1997 Interpretation of large-scale structures observed in a turbulent plane Couette flow. *Intl J. Heat Fluid Flow* **18**, 55-69.

29. PHILLIPS, O. M. 1957 On the generation of waves by a turbulent wind. *J. Fluid Mech.* **2**, 417-445.

30. PHILLIPS, O. M. & KATZ, E. J. 1961 The low frequency components of the spectrum of wind generated waves. *Jour. Marine Res.* **19** 57-69.

31. PHILLIPS, O. M. 1977 *Dynamics of the Upper Ocean.* Cambridge University Press.

32. PLANT, W. J. 1982 A relationship between wind stress and wave slope. *J. Geophys. Res.* **87** 1961-1967.

33. SPALART, P. R., MOSER, R. D. & ROGERS, M. M. 1991 Spectral methods for the Navier-Stokes equations with one infinite and two periodic directions. *J. Comput. Phys.* **96**, 297-324.

34. SULLIVAN, P. P., MCWILLIAMS J. C. & MOENG, C. H. 2000 Simulation of turbulent flow over idealized water waves. *J. Fluid Mech.* **404**, 47-85.

35. SULLIVAN, P. P. & MCWILLIAMS J. C. 2002 Turbulent flow over water waves in the presence of stratification. Phys. Fluids **14**, 1182-1195.

36. SULLIVAN, P. P., MCWILLIAMS J. C. & MELVILLE, W. K. 2004 The oceanic boundary layer driven by wave breaking with stochastic variability. Part 1. Direct numerical simulations. *J. Fluid Mech.* **507**, 143-174.

37. TEIXEIRA, M. A. C., BELCHER, S. E. 2006 On the initiation of surface waves by turbulent shear flow. *Dynamics of Atmospheres Oceans* **41**, 1-27.

38. TOWNSEND, A. A. 1972 Flow in a deep turbulent boundary layer over a surface distorted by water waves. *J. Fluid Mech.* **55**, 719-735.

39. TOWNSEND, A. A. 1980 Sheared turbulence and additional distortion. *J. Fluid Mech.* **98**, 171-191.

40. TSAI, W.-T. & YUE, D. K. P. 1995 Effect of soluble and insoluble surfactant on laminar interactions of vortical flows with a free surface. *J. Fluid Mech.* **289**, 315-349.

41. TSAI, W.-T. 1998 A numerical study of the evolution and structure of a turbulent shear layer under a free surface. *J. Fluid Mech*. **354**, 239-276.

42. TSAI, W.-T., CHEN, S.-M. & MOENG, C.-H. 2005 A numerical study on the evolution and structure of a stress-driven free-surface turbulent shear flow. *J. Fluid Mech.* **545**, 163-192.

43. VAN DUIN, C. A. & JASSEN, P. A. E. M. 1992 An analytic model of the generation of surface gravity waves by turbulent air flow. *J. Fluid Mech.* **236**, 197-215.

44. VERON, F. & MELVILLE, W. K. 2001 Experiments on the stability and transition of wind-driven water surfaces. *J. Fluid Mech.* **446**, 25-65.

45. WEHAUSEN, J.V. & LAITONE, E.V. 1960 Surface waves. In *Handb. Phys.*, **9**, 446-778. Berlin: Springer-Verlag

Vita

February, 1976	Born, Hsinchu, Taiwan (R. O. C.)
1998	B.S. Oceanography
	National Taiwan Ocean University, Taiwan
2000	M.S. Oceanography
	National Taiwan University, Taiwan
2005-2006	Visiting student,
	Mesoscale & Microscale meteorology,
	National Center for Atmospheric Research,
	Boulder, Colorado
2007	Ph.D. Civil Engineering
	National Chiao Tung University, Taiwan